Norwegian University of
Science and Technology

Formation of silicon nanostructures in silicon nitride thin films for use in solar cells

Magnus Boge

Master of Science in Electronics
Submission date: June 2010
Supervisor: Tor A Fjeldly, IET
Co-supervisor: Muhammad Nawaz, IFE

Norwegian University of Science and Technology
Department of Electronics and Telecommunications

Problem Description

Anti-reflective coating (ARC) is used for silicon wafer based solar cells in order to reduce the reflectance at the surface, and to increase amount of light entering the cell that might be absorbed. High energy photons cannot be utilized in the silicon solar cell. Silicon nanoparticles have some interesting properties due to their low dimensionality. One high energy photon absorbed may be transformed to two or more low energy photons, that can be used by the solar cell in a more efficient way.

The goal for this thesis is to develope silicon nitride ARCs containing silicon nanoparticles and also to characterize the films with a focus on ellipsometry.

Assignment given: 15. January 2010
Supervisor: Tor A Fjeldly, IET

Abstract

The increase in the world's demand for energy, and the fact that at one point we will run out of oil and gas which are two major contributers of the world supply of energy toady, are two reasons for why new and reliable energy sources are needed. The solar industry is one of the fastest growing industires, but the price of energy delivered by solar cells is still too high compared to other alternatives. More research is therefore needed in order to drive the price of solar energy down.

In this report seven silicon nitride films with different stoichiometry are deposited on silicon substrate by the plasma enhanced chemical vapor deposition (PECVD) method. The deposition conditions are selected in order to enhance the formation of silicon nanoclusters. Silicon nanostructures have interesting properties due quantum effects observed at these dimensions. The most interesting of these properties is the ability to tune the silicon nanostructures to absrob ligth at different wavelengths. High energy light cannot be utilized in silicon solar cells. With the application of silicon nanostructures, this light can be absorbed and down-converted to usable light which is then transmitted into the solar cell. This would increase the efficiency of the soalr cell, which results in cheaper energy. Two ensembles of as-deposited and annealed (annealed at 1050° C) samples were characterized with different techniques in order to find the thickness, composition, light emitting sources and optical constants of the films. The techniques used were ellipsometry, photo-luminescence (PL) and transmission electron microscopy (TEM).

The results obtained shows that all films are porous (indicated by the low index of refraction). One of the effects of annealing is an increase in the refractive index for all samples, which is an indication that the films have become more compact as a result of the annealing process. PL is obtained for samples with a high flow of ammonia, while samples of a low flow have little or no PL. The annealing process increase the PL observed for samples with a high ammonia flow, while a reduction is observed for the samples with a low flow. TEM images reveals that only one sample has any nanostructures present, so the observed PL is likely related to defect states.

Formation of silicon nanostructures in silicon nitride thin films for use in solar cells

Magnus Boge
magnusbo-at-unik.no

June 18, 2010

Preface

The completion of this thesis also represents a completion of my master's degree at the Norwegian university of science and technology (NTNU) and represents a big accomplishment so far in my life. I am very thankful for the opportunity given to me here at IFE, and for the very interseting topic I was given. I would especially like to thank my supervisors Dr. Jeyanthinath Mayandi and Dr. Sean Erik Foss for their support, guidance and enthusiasm and for always being available for discussions and comments during the work of this thesis. I would also like to thank Annett Thøgersen for the TEM iamges and Dr. Augustinas Galeckas for the PL measurements. Last I would also like to thank the rest of the research group here at IFE for making my time here very pleasant. Thank you!

Kjeller, June, 2010

Magnus Boge

Contents

Preface **i**
List of Figures . . . iv
List of Tables . . . vii

1 Introduction **1**

2 The silicon solar cell **6**
2.1 A brief description of silicon . . . 6
2.2 The silicon solar cell . . . 9
2.3 Anti-reflective coating (ARC) . . . 14
2.4 Basic properties for the silicon nanocrystal . . . 15

3 Experimental details **17**
3.1 Experimental method . . . 17
3.2 Plasma Enhanced Chemical Vapor Deposition (PECVD) . . . 20
3.3 Ellipsometry . . . 21
3.4 Transmission electron microscopy (TEM) . . . 25
3.5 Photo-luminescence (PL) . . . 26

4 Results **27**
4.1 Ellipsometry results . . . 27
4.2 PL measurements . . . 38
4.3 TEM results . . . 44

5 Discussion **48**
5.1 Ellipsometry . . . 48

5.2 PL measurements 54
5.3 TEM images 57

6 Conclusion and further work **59**

Bibliography **61**

A The fit of modelled Ψ and Δ values **67**

B Selected results obtained with the ellipsometry model with a BEMA layer consisting of a T-L oscillator, silicon nitride and voids **75**

C Lifetime measurements for selected samples **84**

List of Figures

1.1 Development of the gross domestic product and energy consumption for the EU between 1995 and 2001 2

2.1 Band structure of silicon, found in [8] 7
2.2 Absorption spectra of Si and GaAs, found in [40] 8
2.3 Relationship between open circuit voltage, short circuit current density and maximum power point, from [40] 10
2.4 The change in minority carriers when the solar cell is illuminated, L_n and L_p are the diffusion lengths for electrons and holes respectively, while $-W_p$ and W_n are the edges of the depletion region in the p-region and the n-region respectively, from [36] 14

3.1 RTA process for annealed samples 19
3.2 Schematic of PECVD system, from [44] 20
3.3 Sketch of ellipsometry model 23

4.1 Optical constants for ammonia level of 7.8 sccm for annealed and as-deposited samples 31
4.2 Optical constants for ammonia level of 10 sccm for annealed and as-deposited samples 32
4.3 Optical constants for ammonia level of 15.6 sccm for annealed and as-deposited samples 33
4.4 Optical constants for ammonia level of 23.4 sccm for annealed and as-deposited samples 34
4.5 Optical constants for ammonia level of 31.2 sccm for annealed and as-deposited samples 35

4.6 Optical constants for ammonia level of 50 sccm for annealed and as-deposited samples 36
4.7 Optical constants for ammonia level of 50 sccm no H_2 for annealed and as-deposited samples 37
4.8 PL measurements at room temperature for as-deposited samples 38
4.9 PL measurements at room temperature for annealed samples . 39
4.10 Temperature dependent PL measurements for as-deposited and annealed sample 7 41
4.11 PL measurements for samples 5, 6 and 7 at 10° K 42
4.12 PL measurements for high sensitivity setup for samples 1-4 . . 43
4.13 TEM image of annealed sample 4 44
4.14 TEM image of annealed sample 5 45
4.15 TEM image of annealed sample 6 45
4.16 TEM image of annealed sample 7 46
4.17 TEM image of as-deposited sample 5 46
4.18 TEM image of as-deposited sample 6 47
4.19 TEM image of as-deposited sample 5, filtered at 21 and 16 eV 47

5.1 Optical constants for silicon 52
5.2 Optical constants for silicon nitride 53

A.1 The fit of Ψ and Δ for ammonia level of 7.8 sccm 67
A.2 The fit of Ψ and Δ for ammonia level of 10 sccm 68
A.3 The fit of Ψ and Δ for ammonia level of 15.6 sccm 68
A.4 The fit of Ψ and Δ for ammonia level of 23.4 sccm 69
A.5 The fit of Ψ and Δ for ammonia level of 31.2 sccm 69
A.6 The fit of Ψ and Δ for ammonia level of 50 sccm 70
A.7 The fit of Ψ and Δ for ammonia level of 50 sccm and no H_2 . 70
A.8 The fit of Ψ and Δ for ammonia level of 7.8 sccm annealed . . 71
A.9 The fit of Ψ and Δ for ammonia level of 10 sccm annealed . . 71
A.10 The fit of Ψ and Δ for ammonia level of 15.6 sccm annealed . 72
A.11 The fit of Ψ and Δ for ammonia level of 23.4 sccm annealed . 72
A.12 The fit of Ψ and Δ for ammonia level of 31.2 sccm annealed . 73
A.13 The fit of Ψ and Δ for ammonia level of 50 sccm annealed . . 73
A.14 The fit of Ψ and Δ for ammonia level of 50 sccm and no H_2 annealed 74

B.1 The fit of Ψ and Δ for ammonia level of 7.8 sccm 76
B.2 The fit of Ψ and Δ for ammonia level of 7.8 sccm, annealed . . 76
B.3 The fit of Ψ and Δ for ammonia level of 23.4 sccm 77
B.4 The fit of Ψ and Δ for ammonia level of 23.4 sccm, annealed . 77

B.5 The fit of Ψ and Δ for ammonia level of 31.2 sccm 78
B.6 The fit of Ψ and Δ for ammonia level of 31.2 sccm, annealed . 78
B.7 The fit of Ψ and Δ for ammonia level of 50 sccm 79
B.8 The fit of Ψ and Δ for ammonia level of 50 sccm, annealed . . 79
B.9 Refractive index and extinction coefficient for ammonia level of 7.8 sccm 80
B.10 Refractive index and extinction coefficient for ammonia level of 23.4 sccm 81
B.11 Refractive index and extinction coefficient for ammonia level of 31.2 sccm 82
B.12 Refractive index and extinction coefficient for ammonia level of 50 sccm 83

C.1 Lifetime measurement for sample with ammonia level of 7.8 sccm 84
C.2 Lifetime measurement for sample with ammonia level of 15.6 sccm 85
C.3 Lifetime measurement for sample with ammonia level of 23.4 sccm 86
C.4 Lifetime measurement for sample with ammonia level of 31.2 sccm 86

List of Tables

1.1 Evolution of silicon solar cell efficiency ($> 1\text{cm}^2$ area) nominally under the IEC 904 global or ASTM E892-87 global AM1.5 spectrum at 25°C and 1000Wm^{-2} illumination intensity. 3

3.1 NH_3 levels 19

4.1 Final values for the four fittable parameters in the Tauc-Lorentz oscillator for the as-deposited samples 28
4.2 Final values for the four fittable parameters in the Tauc-Lorentz oscillator for the annealed samples 28
4.3 Final thickness, weighing of each of the constituents of the BEMA model and MSE for as-deposited samples 29
4.4 Final thickness, weighing of each of the constituents of the BEMA model and MSE for annealed samples 29
4.5 Ratio of thickness between annealed and as-deposited samples 30
4.6 Refractive index for $\lambda = 400$nm 30
4.7 Wavelength for PL peaks, FWHM and counts/sec 40

5.1 Thickness found with both TEM and the ellipsometry model from section 3.3 for selected samples 57
5.2 Thickness found with both TEM and the ellipsometry model from appendix B for selected samples 58

B.1 Final values for the four fittable parameters in the Tauc-Lorentz oscillator for the as-deposited samples (alt. BEMA) 75
B.2 Final values for the four fittable parameters in the Tauc-Lorentz oscillator for the annealed samples (alt. BEMA) 80

B.3 Final thickness, weighing of each of the constituents of the alt. BEMA model and MSE for as-deposited samples 80
B.4 Final thickness, weighing of each of the constituents of the alt. BEMA model and MSE for annealed samples 81

CHAPTER 1

Introduction

The world demand for energy is projected to increases at 1.7 % per year through 2030 according to the International Energy Agency (IEA), [22]. The two major contributors to this increase is the growing world population and the economic growth of developing countries.

It is also stated elsewhere, [51], that a country's gross domestic product per capita is directly proportional to it's energy consumption. So it seems inevitable that the world's demand for energy will increase in the future. The IEA predicts that 90 % of the increase in energy demand up to 2030 will be met by fossil fuels, [22]. Burning fossil fuels releases green house gases into the atmosphere. There is a growing concern regarding the impact of the increase in green house gases emission will have on the planet (the rising of sea levels, melting of the snow caps at the poles and more turbulent weather in general). This have shifted focus towards greener energy sources (wind energy, hydro energy and of course photo-voltaics (PV) to name a few). The graph in figure 1.1 shows the increase in the total energy consumption and the increase in the gross domestic product (GDP) for the European Union between 1995 and 2001.

The p-n junction was discovered by Russel Ohl in the mid-1930s and early 1940s when he was working at Bell Laboratories, [45]. Ohl and his colleagues were investigating the use of silicon rectifiers as radar detectors. In their studies of recrystallized silicon melts they discovered barriers resulting from the impurity segregation during the recrystallization process. Ohl found that when one side of the junction was illuminated (or heated) it reached a nega-

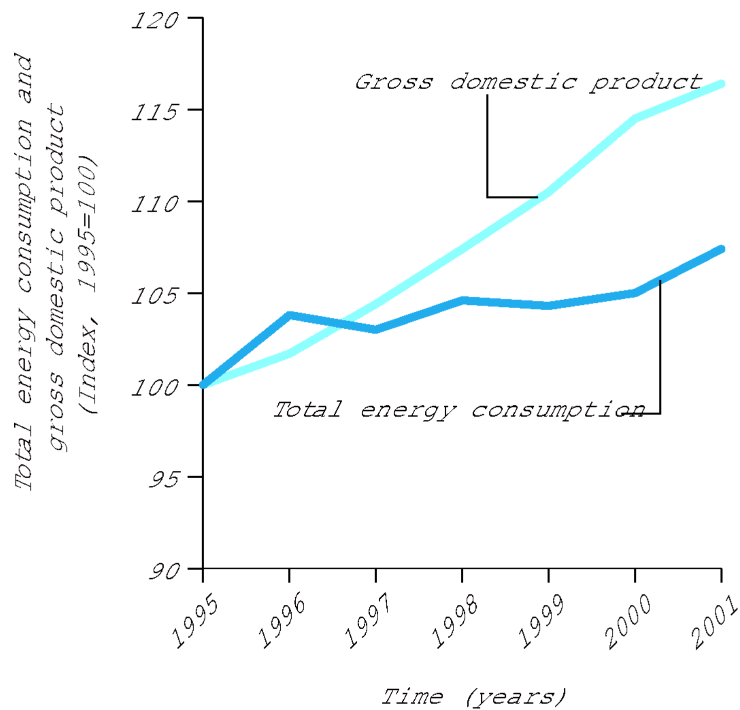

Figure 1.1: Development of the gross domestic product and energy consumption for the EU between 1995 and 2001

tive potential (this region contained phosphorus), and hence the terminology "n-type". The material of opposite type (containing boron) was named "p-type". This first photovoltaic device is believed to have an efficiency below 1%. Tabel 1.1 (refrence [17])shows the evolution of solar cell efficiency until early 1990. As of 2008 a multijunction cell (GaInP/GaAs/GaInAs) have a reported efficiency of 40.8%, [19].

In order for the photovoltaic industry to be able to compete with other energy sources (coal, fossil fuels etc.) more research and developement (R&D) is needed, the incentive for doing more research is largely driven by an economic prospective. The photovoltaic industry is still an expensive alternative compared to the more traditional energy sources (coal, fossil fuels etc.). There have been some government initiatives in several countries to make the photovoltaic industry more competitive, among these are tax-cuts and government subsidies. Countries where the government have had an active role in making the photovoltaic industry more competitive are Germany, Japan, Australia and USA among others. As of 2009 and 2010 there have been sev-

Table 1.1: Evolution of silicon solar cell efficiency ($> 1cm^2$ area) nominally under the IEC 904 global or ASTM E892-87 global AM1.5 spectrum at 25°C and $1000Wm^{-2}$ illumination intensity.

Date	Efficiency(%)	Cell structure	Organization
3/41	< 1	Melt-grown junction	Bell Laboratories
3/52	1	He bombardment	Bell Laboratories
$\sim$ 12/53	$\sim$ 4.5	Li-diffused wraparound	Bell Laboratories
1/54	$\sim$ 6	B-diffused wraparound	Bell Laboratories
11/54	$\sim$ 8	B-diffused wraparound	Bell Laboratories
5/55	$\sim$ 11	B-diffused wraparound	Bell Laboratories
$\sim$ 12/57	12.5	0.5×2cm, B-diffused	Hoffman Electronics
8/59	14	Grid-contact, B-diffused	Hoffman Electronics
8/61	14.5	B-diff. Ar coat, gridded	Commercial, USASRDL
1/73	15.2	Violet cell	Comsat Laboratories
9/74	17.2	Textured non-reflecting	Comsat Laboratories
9/83	18	MINP cell	University of NSW
12/83	18.3	PESC	University of NSW
5/85	19.0	PESC	University of NSW
10/85	20.0	Microgrooved PESC	University of NSW
7/86	20.6	Microgrooved PESC	University of NSW
4/88	20.8	Microgrooved PESC	University of NSW
9/88	22.3	Rear point contact cell	Stanford University
12/89	23.0	PERL cell	University of NSW
2/90	23.3	PERL cell	University of NSW

eral cut-backs in these subsidies, which is believed to cause a reduction in the growth rate for the future demand for solar cells (there will be an overcapacity on the production side of the industry due to the unnatrual demands caused by the stimuli of government subsidies). Some major events that took place in the financial markets in 2008 and 2009 (the collapse of several major banks and insurance companies in the USA), have had a major impact on the economies of most of the countries in the world, and could possibly be one of the reasons for why some governments have decided to cut back on subsidies. Right before the collapse in the summer of 2008, oil prices were soaring at $145 per barrel[1]. The financial crisis led to a significant drop in oil prices, but when the world economy stabilise this could very well lead to an increase in the oil prices. The fluctuating oil prices, the fact that the world at one point will run out of oil and the economic factor already mentioned

[1]http://www.bloomberg.com/apps/news?pid=20601087&sid=aPW1IHcLY51A&refer=home

are all drving forces for why more R&D is needed within the PV industry. As of 2009 the cummulative production of photovoltaic modules was about 21000 MW.[2] There are three ways in which R&D can help make the solar cell a clear alternative to other energy sources and these are:

1. Lower the production costs of solar cells
2. Make the solar cell more efficient
3. A combination of the two

It has been stated in [18] that about 70% of the total cost of a solar cell is related to material cost. Substantial research have been conducted in order to find ways of how to reduce the amount of material used in the production of solar cells. One way of reducing the amount of material is by using thinner wafers. A problem with this approach is that the optical thickness[3] of the silicon wafer needs to be of a substantial length in order for the silicon to be able to absorb the light (silicon is not a very efficient absorber of light, as will be explained in section 2.1). One way of dealing with this problem is to deposit a reflective coating on the backside of the silicon substrate, this will reflect light back into the substrate.

The first reports on luminescence from chemically etched silicon can be found in articles [6] and [12]. This was later called porous silicon. This discovery sparked an interest in finding a way on how to integrate a light emitting silicon structure in the well developed silicon based microelectronic industry. Photoluminescence from *silicon nanocrystals* (nc-Si) embedded in a silicon dioxide (SiO_2) matrix[4] is generally well understood, [21, 9, 55], but silicon dioxide is not well suited to be used as an *anti-reflective coating* (ARC) which is an important part of a solar cell. Silicon nitride on the other hand is already a well developed anti-reflective coating for silicon solar cells. Also when either silane (SiH_4) or ammonia (NH_3) is used as precursor gases, excess hydrogen released during the deposition or annealing process is known to passivate *dangling bonds* in the ARC film, [52, 4]. In this report silicon-nitride ARC's with different stoichiometry are deposited on silicon substrates, the aim is to get an ARC that also contains silicon nanocrystals. Silicon nanocrystals have some interesting properties due to their quantum nature, they behave more like direct gap materials and they may be tuned (by adjusting the size)

[2] http://vitalsigns.worldwatch.org/vs-trend/record-growth-photovoltaic-capacity-and-momentum-builds-concentrating-solar-power

[3] the thickness that light traveling through the wafer "sees"

[4] The surrounding material of the nanocrystals

to emitt light at different wavelengths. Photons with an energy of above 3 eV cannot be utilized in silicon solar cells. These high energy photons will be lost through thermalization within the solar cell. The tunability of the band-gap and the increased absoprtion of the silicon nanocrystals, may be utilized to increase the efficiency of the solar cell by having the silicon nanocrystals absorb the high energy photons (UV-light), down-convert this to red light and emitt this light into the solar cell where it can be absorbed and generate current. This report will focus on verifying the presence of the nc-Si in the deposited silicon-nitride ARC by employing different techniques as will be described in the report.

The remaining of this master thesis will be organized in the following way:

Chapter 2: In this chapter som genral principles of the silicon based solar cell will be introduced.

Chapter 3: This chapter introduces the details of the experiments that was carried out over the course of this master's thesis

Chapter 4: The results obtained from the experiments will be presented and commented.

Chapter 5: The results presented in chapter 4 will be discussed.

Chapter 6: Contains the conclusion with suggestions of further work.

CHAPTER 2

The silicon solar cell

2.1 A brief description of silicon

Silicon (Si) is a chemical element with the atomic number 14, and is what is referred to as a *semiconductor*, it is something in between a metal and an insulator. A semiconductor can be an alloy or made out of one element. The silicon crystal is organized in a diamond structure which has a tetrahedral bonding characteristic. Each of the silicon atoms has 4 nearest neighbors which it is covalently bonded to, [29]. Figure 2.1 shows the band structure of silicon. The maximum of the valence band is located at the Γ point, while the minimum of the conduction band is near the X point. This means that silicon has an *indirect* band gap (of 1.1 eV at room temperature), and hence an inefficient absorber of light compared to *direct* gap materials, e.g. GaAs, this can also be seen in figure 2.2. For a direct gap material, the maximum of the valence band and the minimum of the conduction band occur at the same k value. But silicon fabrication technology is well developed because of the semiconductor industry, the absorption spectrum of silicon has a fairly good match to the solar spectrum, silicon is non-toxic, and there is an abundance of silicon available. From an economic perspective (which is very often the constraining factor when it comes to solar cell design), this makes silicon a good material for solar cells.

In order for a photon to excite an electron from the valence band to the conduction band, a phonon (a quantized crystal vibration) with the correct energy must be available in order to conserve the crystal momentum:

$$\hbar\omega = E_g + \hbar\Omega \tag{2.1}$$

In equation 2.1, $\hbar\Omega$ is the phonon energy, E_g is the energy gap and $\hbar\omega$ is the photon energy.

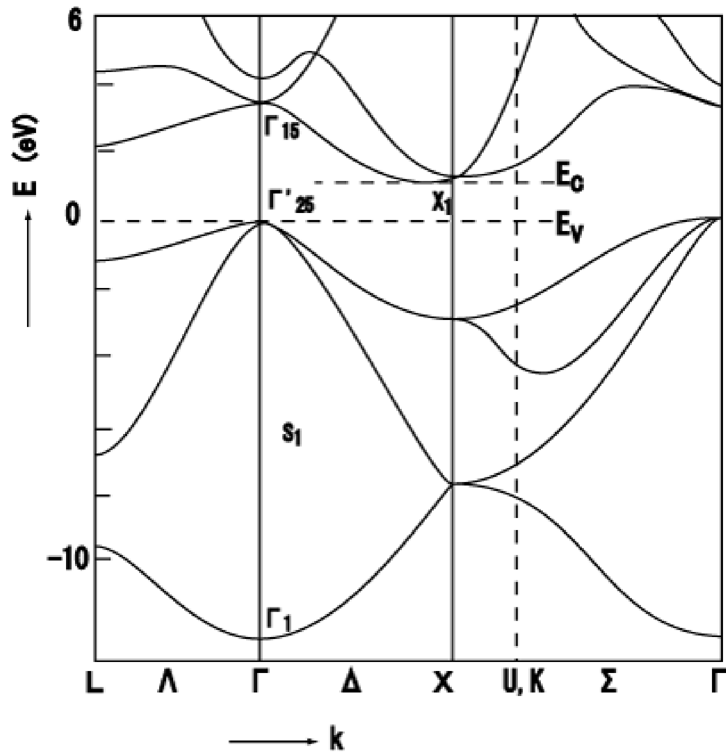

Figure 2.1: Band structure of silicon, found in [8]

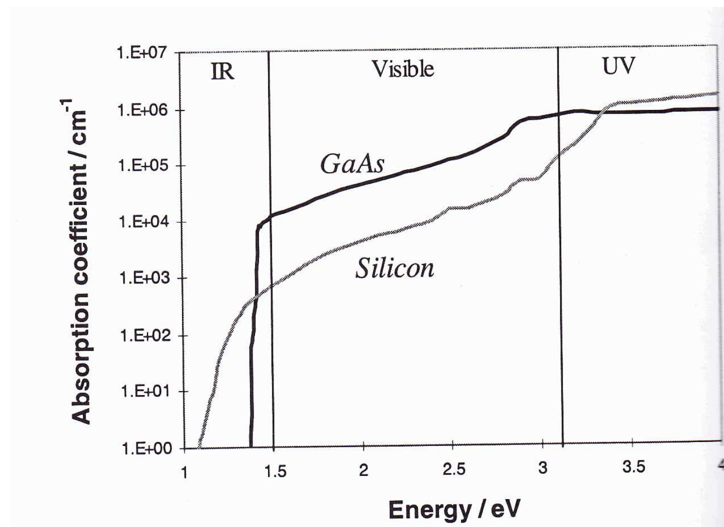

Figure 2.2: Absorption spectra of Si and GaAs, found in [40]

2.2 The silicon solar cell

2.2.1 Photocurrent and efficiency

When silicon is illuminated by the sun, a photocurrent due to the absorbed photon flux may arise. In order to get a photocurrent a *p-n junction* is needed in order to separate the positive and negative charges generated generated by the photon flux. The solar cell also needs to be connected to an external circuit, where the generated current can do electrical work. The photocurrent density is found by integrating the absorbed current density over all energies, [40]:

$$J_{sc} = q \int_0^\infty \eta_c(E)(1 - R(E))a(E)b_s(E)dE \tag{2.2}$$

In equation 2.2, J_{sc} is the short circuit current density (there is no load present), q is the elementary charge, $R(E)$ is the probability of a photon being reflected at the silicon surface, $a(E)$ is the probability of a photon being absorbed by the silicon, $b_s(E)$ is the photon flux from the sun and $\eta_c(E)$ is the probability than an excited electron is being collected. The product $\eta_c(E)(1 - R(E)a(E)$ is known as the cells *quantum efficiency*, $QE(E)$, the probability that an incident photon will deliver one electron to an external circuit. The efficiency of a solar cell is defined as the power density delivered to an external circuit over the incident light power density. The efficiency is related to the short circuit current density (J_{sc}) through the the following relation, [40]:

$$\eta = \frac{J_{sc}V_{oc}FF}{P_s} \tag{2.3}$$

J_{sc} represents the short circuit current density defined in equation 2.2. V_{oc} is the open circuit voltage and FF is the fill factor. At a certain voltage, V_m, the cell reaches its maximum power point with a corresponding current density, J_m. The fill factor is defined as the ratio of J_mV_m over $J_{sc}V_{oc}$. The relationship between the open circuit voltage, the short circuit current density and the maximum power point can be found in figure 2.3.

The maximum theoretical efficiency obtainable for single junction cells, has been found to be equal to 31%. This is known as the *Shockley-Queisser limit* and was calculated by William Shockley and Hans Queisser, [50].

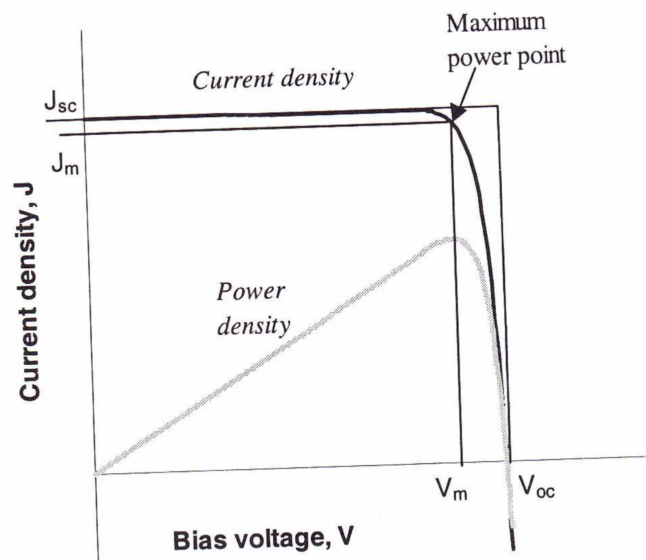

Figure 2.3: Relationship between open circuit voltage, short circuit current density and maximum power point, from [40]

2.2.2 Doping

Silicon material properties can be altered by introducing impurity atoms. When silicon atoms in the crystal lattice is replaced by atoms found in column III or V in the periodic table we get a p-type (column III) or n-type (column V) material. An example of a column III atom is boron which is said to be trivalent, it has 3 electrons in its valence band. In order to complete the bonding to its neighbours it becomes ionized by removing an electron from another bond. This is called an *acceptor* impurity (it accepts an electron). The absence of an electron is referred to as a hole and has a positive charge.

An example of a column V atom is phosphorus, this is a pentavalent atom with 5 electrons in its valence band. When this atom is introduced into the silicon lattice, the bonding to its neighbours can be completed with an excess electron. This is a *donor* impurity (it donates an electron).

The intended introduction of impurities is referred to as *doping*. When impurities are introduced the bonds that make up the crystal are changed, and this changes the energy levels within the crystal. Depending on whether the impurity is p-type or n-type, the Fermi level will also change within the crystal according to the type of doping. To increase the density of positive charges, the crystal is doped p-type. The p-type dopants introduce an acceptor energy level (E_a) that lies just above the valence band (E_v), the Fermi level now lies between the acceptor level and the valence band, because at T = 0°K the acceptor level is empty, and so the Fermi level must lie between the valence band and the acceptor level. The density of negative charge's is increased when the crystal is doped n-type, this introduce a donor energy level (E_d) just below the conduction band. The Fermi level now lies between the donor level and the conduction band because at T = 0°K the donor level is filled. With the increased carrier density, the conductivity of the material is also increased, [36].

2.2.3 p-n junction

The p-n junction is the main bulding block in many electronic devices e.g. transistors, diodes and solar cells. When a p-type and an n-type material are brought in contact, the two materials will form a *p-n junction*. Holes from the p-side will diffuse across to the n-side while electrons from the n-side will diffuse across to the p-side. This is because of the difference in electron- and hole concentrations, known as *concentration gradients*. The holes that

diffuse to the n-region will recombine with electrons and electrons that diffuse to the p-region will recombine with holes. The region near the junction will be depleted of mobile carries, and there will be an electric field in the region that sweeps out carriers that enters the region. *Drift* is a charge's response to an electric field, the direction of the field within the junction will be from the n-region towards the p-region. The electrons will move in opposite direction of the built-in field, while holes will move in the same direction as the field. In thermal equilibrium the diffusion current counterbalances the drift current. The junction work as a barrier for majority carriers (e.g. electrons in the n-region and holes in the p-region), so the solar cell is dominated by minority carrier flow, that is holes in the n-region and electrons in the p-region. The equations for hole- and electron current densities for a junction in thermal equlibrium are given below:

$$J_p(x) = q\left[\mu_p p\mathcal{E} - D_p \nabla p\right] \tag{2.4}$$

$$J_n(x) = q\left[\mu_n n\mathcal{E} + D_n \nabla n\right] \tag{2.5}$$

In equation 2.4 (2.5), μ_p (μ_n) is the hole (electron) mobility, p (n)is the hole (electron) concentration, $\mathcal{E}$ is the electric field and D_p (D_n) is the hole (electron) diffusion coefficient. The p-n junction is typically analyzed with a set of boundary conditions, and with the approximation that the built-in potential due to the electric field is dropped across the depleted region. This is referred to as the *depletion approximation*, ([40], [36]). To generate current that can do work on an external system, the junction (solar cell) needs to be perturbed. Sunlight is an example of such a perturbation. The perturbed carriers, if not collected to do electrical work, will relax back into their equlibrium state, this process is called *recombination.* There are several ways that carriers can recombine. Depending on conditions such as composition of the material, temperature etc. one way of recombination can dominate over the other. The three ways carriers can recombine are:

- **Radiative recombination** in this process an excited electron relax back into the valence band, with the result that a photon with the energy equal to the band gap is released. This process is largley supressed in silicon based solar cells. Because of the indirect gap of silicon, it is required that a phonon with the correct momentum must also be available for the sake of momentum conservation.

- **Auger recombination** in this process two similar carriers collide with the result that one of the carriers is excited to a higher energy level,

while the other recombine with a carrier of opposite polarity. The Auger recombination process is most important when the carrier densities are high.

- **Shockley Read Hall recombination** states found in the band gap of the semiconductor are called defect states and are caused by unwanted impurities. The defect states can capture both electrons and holes, and are typically located in the middle of the band-gap (for the case where the state can only capture one of the two, it is referred to as a trap and slows down carrier transport, these states are usually found relatively close to either the valence band or the conduction band). This is the most important recombination process for silicon solar cells. The Shockley Read Hall recombination is typically approximated by (for p-type material):

$$U_{SRH} \approx \frac{(n - n_0)}{\tau_{n,SRH}} \tag{2.6}$$

  where $n - n_0$ is the excess minority carrier and $\tau_{n,SRH}$ is the minority carrier lifetime.[1]

For a solar cell to be as efficient as possible it is desirable to minimize recombination processes, so that when carriers are generated they will do electrical work. When the solar cell is illuminated, the photon flux will generate carriers and the electric field at the junction will separate the generated electron-hole pair. Under the approximations that the electric field is zero everywhere except in the depleted region and that the recombination is linear in the excess minority carrier concentration, the carrier transport equations can be approximated by the following set of equations[2] (for one dimension):

$$\frac{d^2n}{dx^2} + \frac{q\mathcal{E}}{k_B T}\frac{dn}{dx} - \frac{(n - n_0)}{L_n^2} + \frac{G(x)}{D_n} = 0 \tag{2.7}$$

$$\frac{d^2p}{dx^2} + \frac{q\mathcal{E}}{k_B T}\frac{dp}{dx} - \frac{(p - p_0)}{L_p^2} + \frac{G(x)}{D_p} = 0 \tag{2.8}$$

In both equation 2.7 and 2.8 the last term is the generation term, the third term is recognized as the recombination term, the second term is the drift term and the first term is the diffusion term. L_p and L_n are the diffusion lengths for holes and electrons, and D_p and D_n are the diffusion constants

[1] The time it takes before the carrier will recombine with a carrier of opposite polarity
[2] The relation $\mu = \frac{qD}{k_B T}$, known as Einsteins relation has been used

for holes and electrons. The change in minority carriers when the solar cell is illuminated is pictured in figure 2.4.

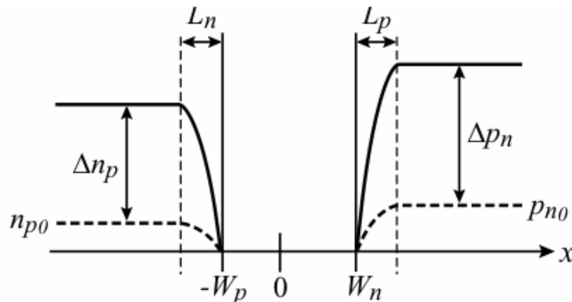

Figure 2.4: The change in minority carriers when the solar cell is illuminated, L_n and L_p are the diffusion lengths for electrons and holes respectively, while $-W_p$ and W_n are the edges of the depletion region in the p-region and the n-region respectively, from [36]

An anology for understanding the importance of minimizing recombination processes can be found in [33]. Here a funnel with water flowing through represents the solar cell (funnel) when illuminated by light (water). The funnel is full of holes of different geometries (e.g. circular, rectangular and triangular) that represents different recombination processes. Water flowing out of the holes is analogous to electrons lost through recombination. At the bottom of the funnel there is a mechanism that lets you controll the amount of water that will flow. When the mechanism is fully open it is a representation of the short circuit current, and when it is fully closed, the water that builds up represents the open circuit voltage.

2.3 Anti-reflective coating (ARC)

It is preferable that the light that is hitting the solar cell is transmitted through the surface of the solar cell so that it can excite carriers that can do electrical work. Silicon has a natural refilectivity of around 40% for visible wavelengths, [40]. Anti-reflective coatings have been developed in order to reduce the reflection. The ARC couples light of preferred wavelength into the solar cell by matching the optical impedance. The ARC typically has an index of refraction between air and that of the solar cell. It has been shown ([35]) that the reflectivity of the ARC (which can be treated as a thin film) is given by:

$$R = \frac{(\eta_0 - \eta_s)^2 + (\eta_0\eta_s/\eta_1 - \eta_1)^2 \tan^2 \delta_1}{(\eta_0 + \eta_s)^2 + (\eta_0\eta_s/\eta_1 + \eta_1)^2 \tan^2 \delta_1} \tag{2.9}$$

where δ_1 is the phase shift in the film, η_0 is the refractive index of air, scaled with respect to the angle of incidence and to whether the light is s-polarized (electric field normal to the plane of incidence) or p-polarized (electric field in the plane of incidence), η_s is the refractive index of the solar cell scaled in the same way as the index of air and η_1 is the index of refraction for the ARC also scaled in the same way is the index of refraction for air. The reflectivity has a minimum when δ_1 is equal to $\frac{\pi}{2}$. The ARC is designed so that the minimum reflectance occurs at a wavelength optimized for maximum utilization of the solar spectrum in the cell (this is typically red light). The incident spectrum from the sun is broad so this means that the ARC will have a higher reflectivity as one move away from the optimized wavelegth. The reflectivity also depends upon angle of incidence, and it will change when the angle is changed. The reflectivity will be zero when the following condition is true:

$$n_1 = \sqrt{n_0 n_s} \tag{2.10}$$

So by having an ARC with the refractive index equal to $\sqrt{n_s}$ the reflectivity can be equal to zero for a given wavelength. The index of refraction for silicon at 1.5eV is around 3.44 so a good ARC should ideally have an index of refraction equal to 1.85. Silicon nitride (Si_3N_4) has an index of refraction which is equal to 1.97 at 1.5eV so it has a good match to the ideal index of refraction for an anti-reflective coating for silicon. Another point that is worth mentioning in this section is the role of hydrogen during deposition of the ARC. At the surface of the (untreated) silicon solar cell there will be *dangling bonds*.[3] These bonds serves as recobination centers or trap states and should be removed. The hydrogen will form a bond with unpaired band, and neutralize the defect. The surface is then said to be *passivated*.

2.4 Basic properties for the silicon nanocrystal

The bulk properties for silicon are well understood, and a brief description is found in 2.1, when silicon is scaled down in size (essentially down to the nanoscale) it will start to exhibit different properties to that of bulk silicon. The energy levels found in the valence and conduction band of bulk silicon

[3] A Si atom that is only bonded to three other Si atoms, this leaves one valence electron that is not involved in bonding

are treated as a continuum of energy levels because the limits in the x, y and z direction are treated as infinity. This is not a problem because the bulk silicon is comprised of so many silicon atoms that the quantized energy levels you find in a single silicon atom will essentially be a continuum of energy levels. For nanocrystals, this is no longer the case. Because of the finite dimension in one, two or all of the directions x, y and z, the energy levels in the bands will be discrete and the carriers will be confined. One of the effects observed for Si at the nanoscale is the increase in absorption for certain wavelengths, [32], it seems like the silicon has become a direct material. This can partially be attributed to the Heisenberg uncertainty principle;

$$\Delta x \Delta p \geq \frac{\hbar}{2} \tag{2.11}$$

This simply states the the product of the uncertainty in position and the uncertainty in momentum has to be equal to or greater than the reduced Planck constant divided by two. When the silicon is reduced in size, the uncertainty in position for a carrier is reduced, this gives an increase in the uncertainty of the momentum, or stated in another way; as the carriers are confined in real space, their wavefunctions spread out in momentum space and the electron-hole wavefunction overlap is greater. This is the main reason for why silicon nanoparticles behaves more like a direct material. Another feature of silicon nanoparticles is that the particles will emitt light with different wavlengths depending on the size of the particles. An approach on how to explain this can be done by treating the nanoparticles and the discrete energy levels in the valence and conduction band as a box surrounded by infinite potential walls (this is definitely not the case but it will suffice for the sake of this simplified example). A reduction in size will increase the distance between the valence- and conduction band, i.e an increase in the band gap. An increase in size will have the opposite effect, a reduction in the band-gap until the band-gap is equal to that of bulk silicon. The quantized energy levels will be on the form:

$$E_n = \frac{n^2 \pi^2 h^2}{2mR^2} \tag{2.12}$$

where $n = 1, 2, 3...$, m is the mass of the particle and R is the width of the well. A more rigorous treatment of the quantum confinement factor of the nanoparticles and the size dependent luminescence effect can be found in [32], [53], [48], [13] and [31].

CHAPTER 3

Experimental details

This chapter will describe the experimental details and the equipment used. The plasma enhanced chemical vapour deposition (PECVD) method used for depositing the ARC will be briefly described, as will the transmission electron microscopy (TEM) and photo-luminescence (PL) meaurements. The ellipsometer will be described in more detail, a lot of time was invested in getting a good model based on the optical measurments from the ellipsometer.

3.1 Experimental method

Seven different silicon nitride films were deposited on a polished <1 0 0> p-type (Boron doped) Si substrate, 4" and $275-325\mu$m thick by the rf PECVD method. The resistivity of the Si substrates were $1-3\Omega \cdot cm$. The composition of the films were altered by changing the levels of NH_3. The NH_3 levels (unit of standard cubic centimeters per minute (sccm)) can be found in table 3.1. The 4" wafers were cut into 4 pieces. A total of 21 samples were prepared, 14 of the samples recieved the PECVD treatment on both sides (double side), the reason for depositing the film on both sides was to be able to measure the lifetime of carriers. The remaining 7 samples were only treated on one side. The SiH_4 level was set to 15.6 sccm for all samples, while the H_2 level was set to 50 sccm for all samples except for sample 7 were the H_2 level was set to 0. The chamber pressure was set to 300 mTorr for all samples and the rf power was set to 50 W for all samples. The rf frequency was set to 13.56 MHz for all samples. All samples were etched in 5% HF for 2 minutes

before deposition, and the deposition time was set to 5:00 min for all samples. The substrate temperature was set to 300°C for all samples. The aim for all samples was a film thickness of 80 nm. After deposition, ellipsometer measurements were carried out on the single side samples. This was done in order to determine the optical constants of the film. The measurements were carried out with a spectroscopic ellipsometer desgined by J.A. Woollam Co.,Inc. The WVASE32 software was used to determine the optical constants of the films. The single side samples were then cut in half, one of the halves were then cut in smaller pieces, the smaller pieces were numbered and then annealed. The rapid thermal annealing (RTA) process can be found in figure 3.1. The RTA process took place in an argon (Ar) ambient, quartz chamber. The chamber was first ramped up to a temperature of 700° C and kept at this temperature for 25 seconds. This was done in order to remove contamination that might be present on the sample or in the chamber, any residual moisture if present will also be removed. The temperature was then ramped up to 1050° C, the samples were kept at this temperature for 20 seconds, and then cooled down to room temperature. One reason for why the samples are annealed is because Si-rich dielectrics are known to decompose into two phases as a result of annealing; Si clusters and a matrix. The driving force behind the transformation is the reduction in free energy as stated in [43] and [10].

Photo-luminescence (PL) measurments were carried out at the university of Oslo (UiO) for selected samples (both annealed and the as-deposited samples) by Augustinas Galeckas. An excitation source of 325 nm was used for the room temperature PL measurements. Three pairs of annealed and as-deposited samples were selected for another round of PL measurements. This time the excitation source was kept at 325 nm, while the temperature was changed. The temperature was increased from 10° K to room temperature. Based on the results from PL measurements, six samples (pairs of annealed and as-deposited) were selected for Transmission Electron Microscopy measurements (TEM), this was also carried out at UiO by Annett Thøgersen. After examining the results from the PL measurements an additional sample (sample 4 annealed) was also included for the TEM measurements.

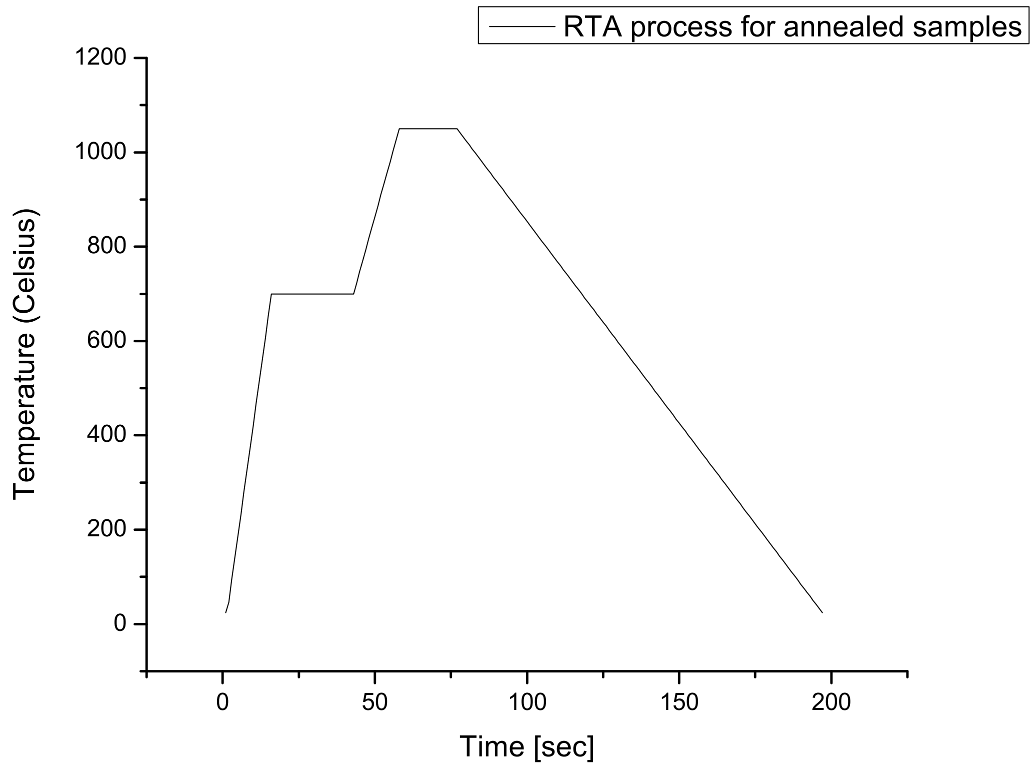

Figure 3.1: RTA process for annealed samples

Table 3.1: NH_3 levels

Sample #	NH_3 level [sccm]
1	7.8
2	10
3	15.6
4	23.4
5	31.2
6	50
7	50 (no H_2)

3.2 Plasma Enhanced Chemical Vapor Deposition (PECVD)

PECVD is performed in a vacuum chamber. The process takes place between two parallel conducting plates, the position of the plates may be changed in order to optimize the deposition process. The wafer is typically placed in a vacuum chuck on the bottom electrode and rf (radio frequency) power is applied to the top electrode. A plasma[1] is created when the source gas is introduced into the chamber, the exhaust gas is usually pumped out beneath the bottom electrode. Most PECVD systems are cold-wall reactors, this has the advantage that fewer particles will contaminate the reactor walls (as opposed to a hot-wall reactor) so less downtime is required for cleaning. The wafer is then heated. A schematic of a typical PECVD system can be found in figure 3.2.

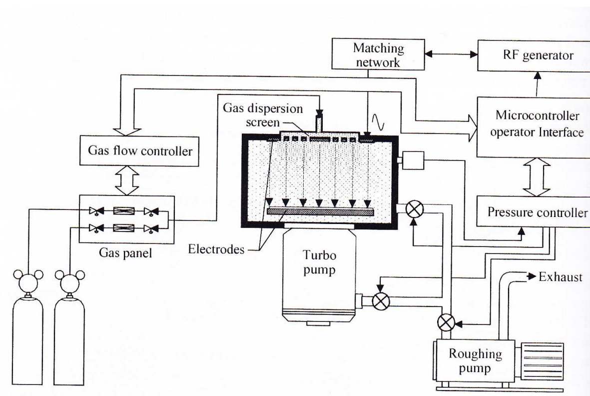

Figure 3.2: Schematic of PECVD system, from [44]

When nitride is deposited with either silane (SiH_4) or ammonia (NH_3) or both as precursor gases it is sometmes written $Si_xN_yH_z$ (stoichiometric nitride has the composition Si_3N_4) this is to highlight the fact that films deposited with a source that has a high concentration of hydrogen usually contains hydrogen (for silicon solar cells this is usually not regarded as a problem because of the passivating properties of hydrogen). A more detailed description of PECVD can be found in [5, 44]. A typical reaction equation for the deposition of nitride is:

$$SiH_4 + NH_3 \rightarrow Si_xN_yH_z + H_2 \tag{3.1}$$

[1]A plasma is a medium with equal concentration of positive and negative charges, of which at least one charge type is mobile

3.3 Ellipsometry

Ellipsometry measurements measures the change in polarization when light is reflected from a surface. The ellipsometer measures the change in Ψ and Δ. The relationship between Ψ and Δ is given by:

$$\rho = \tan(\Psi)\exp(i\Delta) = \frac{\tilde{R}_p}{\tilde{R}_s} \tag{3.2}$$

where 3.2 ρ is the magnitude of the reflection coefficient, $\tilde{R}_p$ is the complex reflection coefficient for the p-polarized light and $\tilde{R}_s$ is the complex reflection coefficient for the s-polarized light.When performing ellipsometry measurments one typically wants to find the thickness of the film that has been deposited, the optical constants of the film, or both. For structures that consists of several layers (which is typically the case) regression analysis is used to account for the reflection from multiple layers. This is also known as an inverse problem. To obtain the optical constants which will be on the form $n + ik = \sqrt{\tilde{\varepsilon}}$ (the right term is the square root of the complex dielectric function), one has to build a model in the software (WVASE32) that comes with the ellipsometer, the response from the model is then calculated and compared with the measured data. This is referred to as "fitting the model to the data". If the fit is bad, the model needs to be changed and a new fit is performed. This process continues until a model that has a satisfying fit to the measured data is obtained.

A typical figure of merit that is given to determine the goodness of fit is the mean squared error (MSE). The formula for determining the MSE is given below:

$$MSE = \frac{1}{2N - M}\sum_{i=1}^{N}\left[\left(\frac{\Psi_i^{mod} - \Psi_i^{exp}}{\sigma_{\Psi,i}^{exp}}\right)^2 + \left(\frac{\Delta_i^{mod} - \Delta_i^{exp}}{\sigma_{\Delta,i}^{exp}}\right)^2\right] \tag{3.3}$$

where N is the number of (Ψ, Δ) pairs, M is the number of variable parameters in the model and σ are the standard deviations on the experimental data. For a noisy measurements, the corresponding standard deviation will be large and that measurement will not be strongly weighted in the fit. Generally one can say that an MSE below 10 is an indication of a model that is well fitted to the experimental data, but this should not be taken as an absolute as the MSE depends upon the complexity of the model and the material of the film. This is different to the χ^2 method, were values around

$\chi^2 = 1$ indicates a good fit for the model. The formula for the MSE, the magnitude of the reflection coefficient and the comments were found in the instruction manual that came with the ellipsometry.

The software (WVASE32) that is used to build the model comes with a vast variety of tabulated values for different materials. The software also comes with specialized layers (e.g Cauchy layer, Tauc-Lorentz layer, effective medium approxiamtion layer) that can be very important when building a good model based on ellipsometry measurements. A big challenge with this experiment was that when the model was built in the software, no other experiments had been conducted on the samples, so there were many unknowns (e.g. film thickness, stoichiometry of the film). Based on an article written by *Filonovich et al.*, [16] were a very detailed and good model was built, the *Bruggeman effective medium approximation* (BEMA) layer seemed like a good candidate to start with. With the changing ammonia level, the stoichiometry of the film will also change. The BEMA layer may account for this by being comprised of up to three different materials, the weighing of each of the materials can change in order to best fit the experimental data. The effective medium approximation represents a reasonable way to mix optical constants together. A more detailed description of the effective medium approximation can be found in [1]. The Bruggeman effective medium approximation is described by the following equation (taken from the instruction manual that comes with the ellipsometer):

$$f_A \frac{\tilde{\varepsilon}_A - \tilde{\varepsilon}}{\tilde{\varepsilon}_A + 2\tilde{\varepsilon}} + f_B \frac{\tilde{\varepsilon}_B - \tilde{\varepsilon}}{\tilde{\varepsilon}_B + 2\tilde{\varepsilon}} + f_C \frac{\tilde{\varepsilon}_C - \tilde{\varepsilon}}{\tilde{\varepsilon}_C + 2\tilde{\varepsilon}} = 0 \tag{3.4}$$

where f_A, f_B and f_C are the volume fractions of constituents A, B and C. $\tilde{\varepsilon}_A$, $\tilde{\varepsilon}_B$ and $\tilde{\varepsilon}_C$ are the complex dielectric functions of constituents A, B and C and $\tilde{\varepsilon}$ is the complex dielectric function of the effective media. This equation will yield an infinite number of solutions, so the software used must be able to correctly choose the appropriate solution. Several combinations of different materials were tried out in the BEMA model and fitted to the experimental data for some of the samples. The materials that were tried were amorphous silicon, crystalline silicon, voids and stoichiometric silicon nitride. The reason for why these materials were selected was again because of the precursor gases used. Any excess silicon present in the film could be described by either the amorphous silicon or the crystalline silicon. The state (crystalline or amorphous) of any excess silicon was unknown, as no other experiments had been performed on the samples at the time. An ideal material to use in the BEMA layer might have been silicon nanocrystals. But the

properties of silicon nanocrystals changes with size, so it will be very difficult to get tabulated values where the size effects can be accounted for. A search in the litterarture did not yield any results regarding tabulated values for silicon nanocrystals. After some rounds with trial and error in seemd like crystalline silicon would yield the best fit to the experimental data, but the overall results were deemed inadequate.

There are several articles [25, 23, 11] were the use of a *Tauc-Lorentz oscillator* (T-L) have been successfully deployed to describe the optical behaviour of stoichiometric silicon nitride, based on this another approach was set forth. This time the T-L oscillator was used as a starting point for the model. Both the T-L oscillator and further development of the model will be described later in this section.

The ellipsometry measurements were carried out on a J. A. Woollam V-VASE spectroscopic ellipsometer with wavelengths ranging between 300-1000 nm, three different angles of incidence were used; 65°, 70° and 75°. A general model was found for all the samples, the model consists of four layers were the bottom layer is the silicon substrate, the next layer is a Tauc-Lorentz oscillator, [24], with zero thickness and it is coupled to the next layer which is a Bruggeman effective medium approximation layer, [3]. This layer is comprised of three parts; one is the T-L oscillator, the other two are crystalline silicon and voids. The weighing of the three constituents depends upon the composition of the material. The final layer is a surface roughening layer which consists of 50% voids and 50% of the underlying material (in this case the BEMA model). Figure 3.3 shows a sketch of the layers that the model is comprised of.

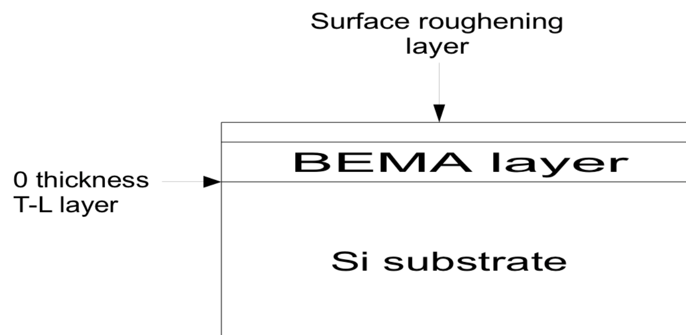

Figure 3.3: Sketch of ellipsometry model

The T-L oscillator is given by the Lorentz formula for oscillating noninteracting atoms, [46], multiplied by the Tauc joint density of states:

$$\epsilon_{2TL}(E) = \frac{AE_0C(E - E_g)^2}{(E^2 - E_0^2)^2 + C^2E^2}\frac{1}{E} \tag{3.5}$$

The fittable parameters in equation 3.5 are the amplitude A, the band gap E_g, the resonant energy E_0 and a broadening factor C. The real part of the complex dielectric function can be found by the Kramers-Kronig[2] integration:

$$\epsilon_1(E) = \epsilon_1(\infty) + \left(\frac{2}{\pi}\right) P \int_{E_g}^{\infty} \frac{\xi\epsilon_2(\xi)}{\xi^2 - E^2} d\xi \tag{3.6}$$

To get a good fit the starting point before the fit is perfromed typically needs to be relatively close to the final result. If the deviation between the model and the measured data is too big to begin with the final result will not be good (the experience during this experiment is that he final result will be something that does not resemble the measured data at all). The software comes with example files of already known structures, this was very helpful in getting a good starting point for the samples in this experiment. The example file that was used for this experiment was the stoichiometric nitride file. The T-L oscillator was fitted to the tabulated nitride, before the first set of measured data was loaded. The first set of measured data that is loaded must be a set that is relatively close matched to stoichiometric nitride. After some rounds of trial and error, the sample with an ammonia level of 50 sccm (sample 6, table 3.1) was selected as the first sample. The T-L oscillator was then fitted to the measured data and saved. The next sample was the sample with ammonia level of 31.2 sccm (sample 5), the previously saved model for sample 6 was loaded and fitted to the measured data and then saved. The T-L oscillator was fitted to the consecutive samples (4-1) in the same way. Samples 7 was also fitted with the fitted model for sample 6 as a starting point and then saved. The constant term, $\epsilon_1(\infty)$, found in equation 3.6 was set equal to 1 for all samples. The BEMA layer was then applied to the model, the BEMA layer was fitted by first determining the thickness of the film. The initial guess for the thickness of all of the films was 80 nm, as this was the ideal thickness for all of the films. To determine the thickness of the films, the range of wavelengths was limited to a region of long wavelengths (600-800 nm). After the thickness had been determined, the BEMA layer was fitted to the whole spectrum (300-1000nm). The surface roughening layer was applied on top of the BEMA layer, before a final fit was

[2]The Kramers-Kronig relation comes from the requirement that a material cannot respond to an applied electric field prior to the application of the field

performed. An important note on the fitting procedure is that in order to get a good fit for both as-deposited and annealed films the thickness of the film had to be kept as a fittable parameter in both cases in order to get a good fit.

Based on the results obtained from the model described, another model was constructed. The new model is almost identical to the model already described, the only difference being that the crystalline silicon in the BEMA layer was replaced with stoichiometric silicon nitride (Si_3N_4, refrence [20]). The fitting procedure is also changed. The T-L oscillator that was fitted to the as-deposited sample 1 is used as a starting point for the as-deposited sample 1in the new model. Before a fit was performed the BEMA layer now consisting of the T-L oscillator, silicon nitride and voids was applied. A limited range of wavelengths (600-800 nm) was again selected for determining the thickness (because of the uncertainties in the previous model, it was decided to use the thickness as a fit parameter in this model as well). After the thickness had been determined, the model was fitted for the whole spectrum (300-1000 nm), a surface roughening layer was applied before a final fit was performed. This model was saved and the applied to sample 2, which followed the same procedure by first using a restricted range of wavlengths to detemine the thickness and then fitting the model to the whole spectrum. The remaining samples were fitted using this procedure. Results for selected samples (both as-deposited and annealed) can be found in appendix B.

3.4 Transmission electron microscopy (TEM)

For transmission electron microscopy (TEM), the limiting resolving power is set by the wavelength of the accelerated elecrtrons. The theoretical resolving power of a TEM is subatomic, but due to imperfections (e.g. imperfections in the lenses) the actual limit is in the region of ~1 nm. In a TEM the electron beam travels through the sample and is detected on the back side of the sample. This means that the sample needs to be thin in order for the beam to be able to penetrate the sample, the thickness can typically not exceed hundreds of nanometers. The samples were prepared at UiO by the following procedure: Cross-sectional TEM samples were prepared by ion-milling[3] using a Gatan precision ion polishing system with 5 kV gun voltage. The samples were analysed by HRTEM (High Resolution TEM), EDS (Electron Dispersive Spectroscopy), EFTEM (Energy Filtered TEM) and EELS (Electron Energy Loss Spectroscopy) in a 200 keV JEOL 2010F

[3] Ion milling is a mechanical process that uses a noble gas to etch a target sample. The process is sometimes referred to as the micromechanical analog of sandblasting

microscope with a Gatan imaging filter and detector, and a NORAN Vantage DI+ EDS system.

3.5 Photo-luminescence (PL)

Photoluminescence (PL) is a process were a photon is absorbed, this creates an electron-hole pair, the electron-hole pair will then recombine either radiatively or non-radiatively. The excitation source is typically a laser operating at a wavelength of either $\lambda = 325$ nm or $\lambda = 488$ nm. Photons from the excitation source will create electron-hole pairs within the sample. The excited carriers will relax back into their equilibrium position through one of several recombination processes. Some of these processes are non-radiative (recombination centers in the band-gap/interfaces or Auger) others are radiative. The electron can decay from the conduction band back to the valence band releasing a photon in the process that is equal to the band-gap, or the recombination can take place at interface states or via trap states found in the band-gap. In either case, the energy emitted or given up will be equal to the difference between the two energy states. A typical PL setup has a laser light source followed by a filter that removes unwanted frequencies. The beam will then hit the sample, the reflected/emitted light is passed through a monochromator[4]. The light is then passed on to a photon-detector before it is amplifiend and finally analyzed by a computer. A PL spectra may then be created.

[4] A monochromator is an optical device that transmits a narrow band of wavelengths that have been filtered by a grid. The input source at the grid is usually made of a wide range of wavelengths

CHAPTER 4

Results

In this section the results from the ellipsometry measurements, PL measurements and TEM measurements will be presented and commented.

4.1 Ellipsometry results

The optical constants found from ellipsometry measurements can be found in figures 4.1-4.7, while the fit for each model can be found in appendix A. The results for the BEMA model containing nitride can be found in appendix B. By looking at the fit for the as-deposited samples in appendix A it is clear that the overall fit is good, but that the model have a problem in describing the experimental data in areas with kinks. Kinks occur at $\sim$ 380nm for both Δ and Ψ experimental values, there is also a kink at $\sim$ 500nm for he experimental Δ values. This is the case for all samples except for sample 7 where there is also a kink at $\sim$ 900nm. For sample 5 and 6 the fit is better for the experimental data for Ψ at $\sim$ 380nm. One exception is found for sample 4 between the experimental value of Δ at an angle of incidence of 75°. For the kink at $\sim$ 300nm it is as if the modell and the experimental value is inverted with respect to each other. This exception is seen up until $\sim$ 380nm. For the annealed samples, the situation is a little different. For sample 1 and 2 the fit is good for the whole range of wavelengths, there are no kinks in the experimental values of the two samples and the model have no problem in describing the experimental values for the whole range of wavelengths. For sample 3 there is again a kink at $\sim$ 400nm and the model

is not able to accurately describe the experimental data in this area. For sample 4 there is a kink at $\sim$ 350nm and at $\sim$ 460nm for the experimental Δ values. For sample 5 and 6 there is a kink at $\sim$ 350nm, there is also a kink at $\sim$ 550nm (sample 5) and $\sim$ 620nm (sample 6) for the experimental Δ values. A kink for the experimental Ψ values is also starting to form at the respective wavelengths. Sample 7 has three kinks, one at $\sim$ 320nm, one at $\sim$ 440nm and one at $\sim$ 840nm for the experimental Δ values. The final values for the four fittable parameters in the T-L oscillator can be found in tables 4.1 and 4.2 for the as-deposited and annealed samples respectively. The final values for the thickness, the weighing of each of the constituents of the BEMA model and the MSE (mean squared error) can be found in tables 4.3 and 4.4 for the as-deposited and annealed samples respectively.

Table 4.1: Final values for the four fittable parameters in the Tauc-Lorentz oscillator for the as-deposited samples

Sample #	A	E_g	E_0	C
1	81.26	1.97	3.94	3.11
2	65.01	1.86	4.00	2.80
3	78.91	1.68	4.26	2.16
4	97.92	1.45	6.74	3.12
5	18.62	2.24	5.65	2.12
6	74.99	2.77	8.43	3.82
7	51.91	2.64	7.21	2.89

Table 4.2: Final values for the four fittable parameters in the Tauc-Lorentz oscillator for the annealed samples

Sample #	A	E_g	E_0	C
1	348.03	1.50	3.24	2.04
2	398.90	1.50	3.34	2.21
3	257.02	1.44	3.81	2.61
4	145.82	1.04	5.16	3.12
5	5.35	0.02	4.70	2.04
6	26.71	1.33	7.99	1.22
7	28.02	2.42	5.99	2.37

There are several comments to be made about the results that are presented in tables 4.1-4.4. The most obvious is the fact that the thickness changes between the as-deposited samples and the annealed. A ratio of

Table 4.3: Final thickness, weighing of each of the constituents of the BEMA model and MSE for as-deposited samples

Sample #	film thickness [nm]	MSE	*Tauc-Lorentz* (%)	*voids* (%)	*crystalline silicon* (%)
1	50	4.68	95.27	0.98	3.74
2	59	7.62	71.27	22.13	6.60
3	54	6.22	51.08	47.52	1.40
4	63	7.00	39.63	52.80	7.56
5	76	6.66	95.64	0.20	4.16
6	102	5.77	82.50	17.40	0.10
7	141	6.00	67.93	33.58	-1.50

Table 4.4: Final thickness, weighing of each of the constituents of the BEMA model and MSE for annealed samples

Sample #	film thickness [nm]	MSE	*Tauc-Lorentz* (%)	*voids* (%)	*crystalline silicon* (%)
1	44	5.53	44.26	52.03	3.71
2	52	5.65	38.85	55.72	5.44
3	47	5.45	41.32	56.21	2.46
4	56	5.74	38.00	56.99	5.00
5	72	6.23	66.14	28.39	5.47
6	90	8.22	82.19	15.02	2.79
7	127	10.88	66.69	34.40	-1.09

thickness between the annealed and as-deposited samples can be found in 4.5. Inspection of this table reveals that the ratio of thickness for all samples is around 12 %, except for sample 5 where the change is only 5 %. The change in the weighing of the constituents of the BEMA model is also changing between the as-deposited and annealed samples, except for sample 6 where there is only a small change in the weighing of voids and crystalline silicon. It is also worth pointing out that the weighing of crystalline silicon is negative for both as-deposited and annealed samples 7. This does not mean that the result is non-physical, since it is only the weighing in the BEMA model and not the actual percentage of silicon in the film. As for tables 4.1 and 4.2 both the broadening term (C) and the resonant energy (E_0) only changes slightly between the as-deposited and annealed samples. Thers is also a slight change in the energy gap (E_g), the trend is a reduction between the as-deposited and annealed samples. The change in the amplitude is different, for samples 1-3 the change between the as-deposited and annealed is very large (more than 6 times for the biggest change), and the increase is found in the annealed samples. For sample four the change is less than 2

times and the annealed sample has the bigger amplitude. For sample 5, 6 and 7 it is the other way round, the bigger amplitude is found for the as-deposited samples, the change is smaller though, at most 3 times found for sample 5. There is one exception that is worth pointing out and that is the energy gap (E_g) for sample 5. The as-deposited sample has an energy gap of 2.24 eV, while the annealed sample has an energy gap of 0.02 eV, this does not follow the general trend found for the other samples.

Table 4.5: Ratio of thickness between annealed and as-deposited samples

Sample #	Ratio [%]
1	12
2	12
3	13
4	11
5	5
6	12
7	10

The refractive index for all samples for a selected wavelength ($\lambda = 400$nm) can be found in table 4.6. The observed trend here is an increase in the refractive index for annealed samples. It is also clear that an increase in the ammonia level results in a lower refractive index.

Table 4.6: Refractive index for $\lambda = 400$nm

Sample #	$n_{as-deposited}$	$n_{annealed}$
1	3.11	3.39
2	2.86	3.30
3	2.57	2.95
4	2.25	2.51
5	2.11	2.30
6	1.98	2.09
7	1.92	2.02

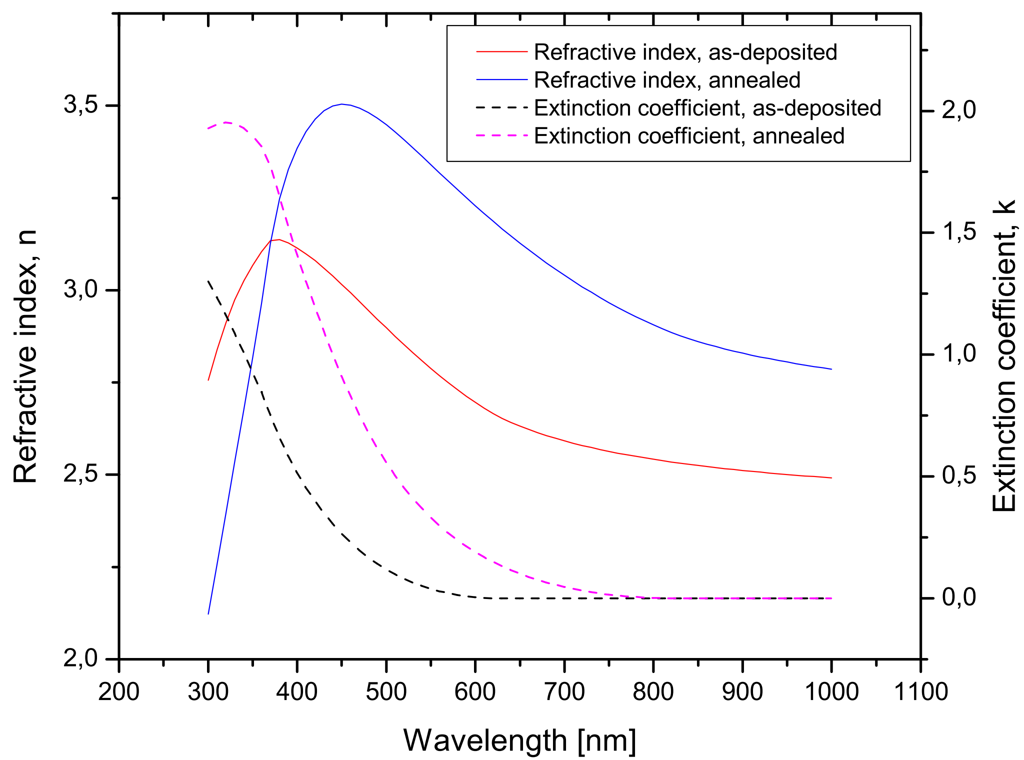

Figure 4.1: Optical constants for ammonia level of 7.8 sccm for annealed and as-deposited samples

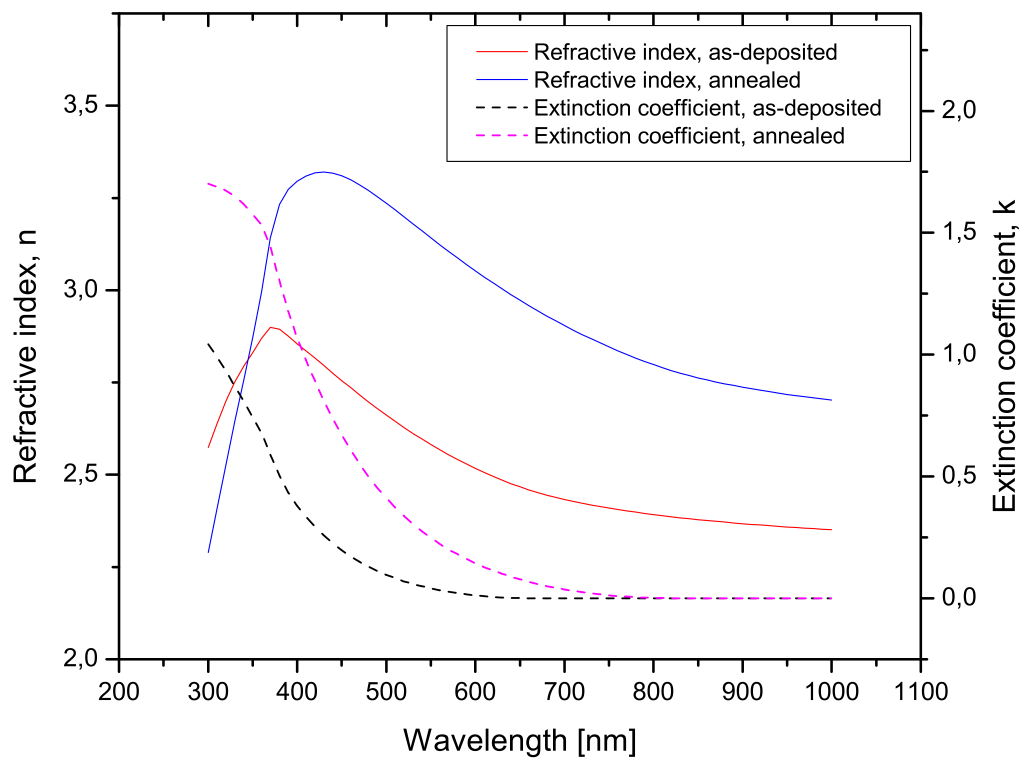

Figure 4.2: Optical constants for ammonia level of 10 sccm for annealed and as-deposited samples

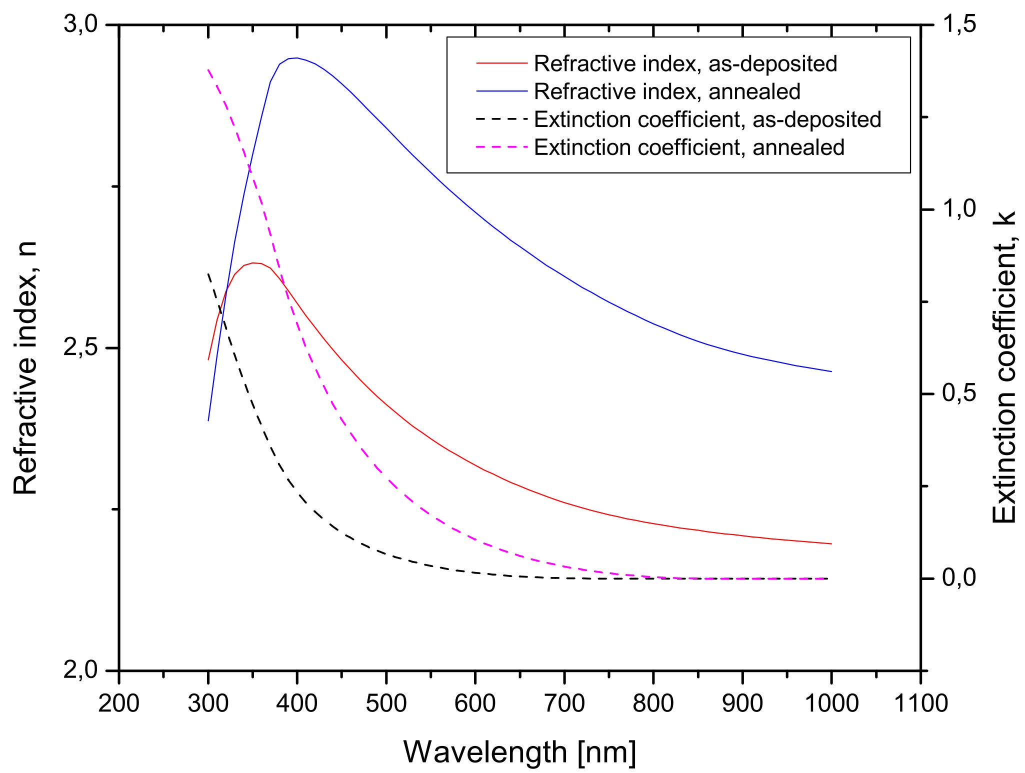

Figure 4.3: Optical constants for ammonia level of 15.6 sccm for annealed and as-deposited samples

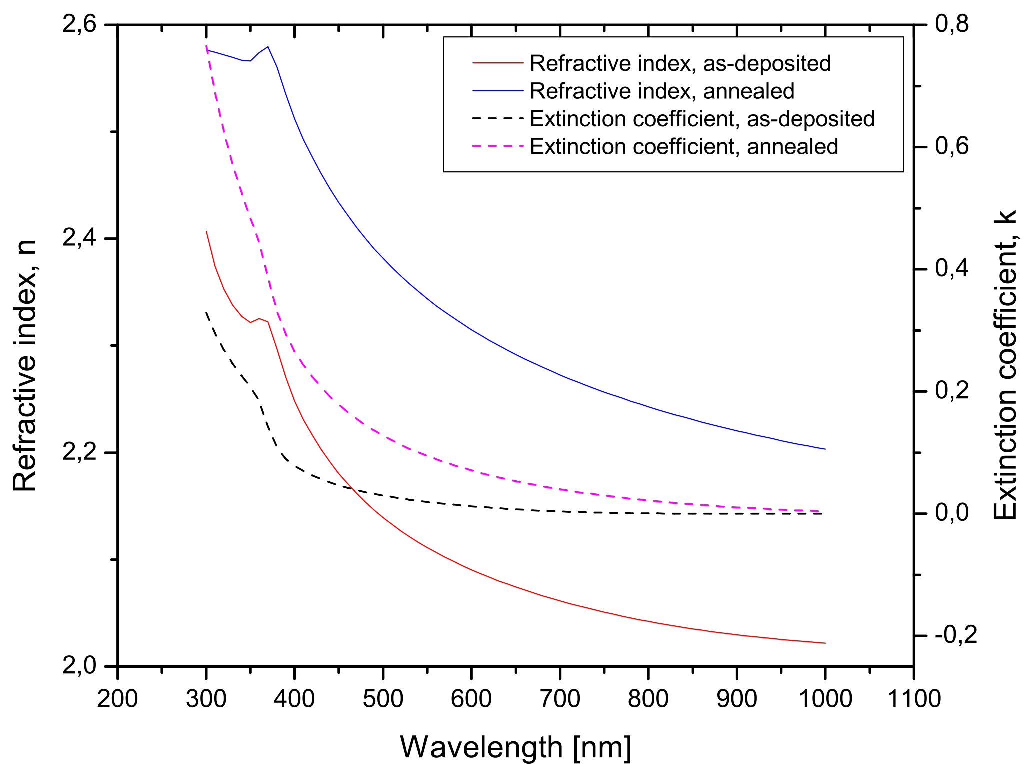

Figure 4.4: Optical constants for ammonia level of 23.4 sccm for annealed and as-deposited samples

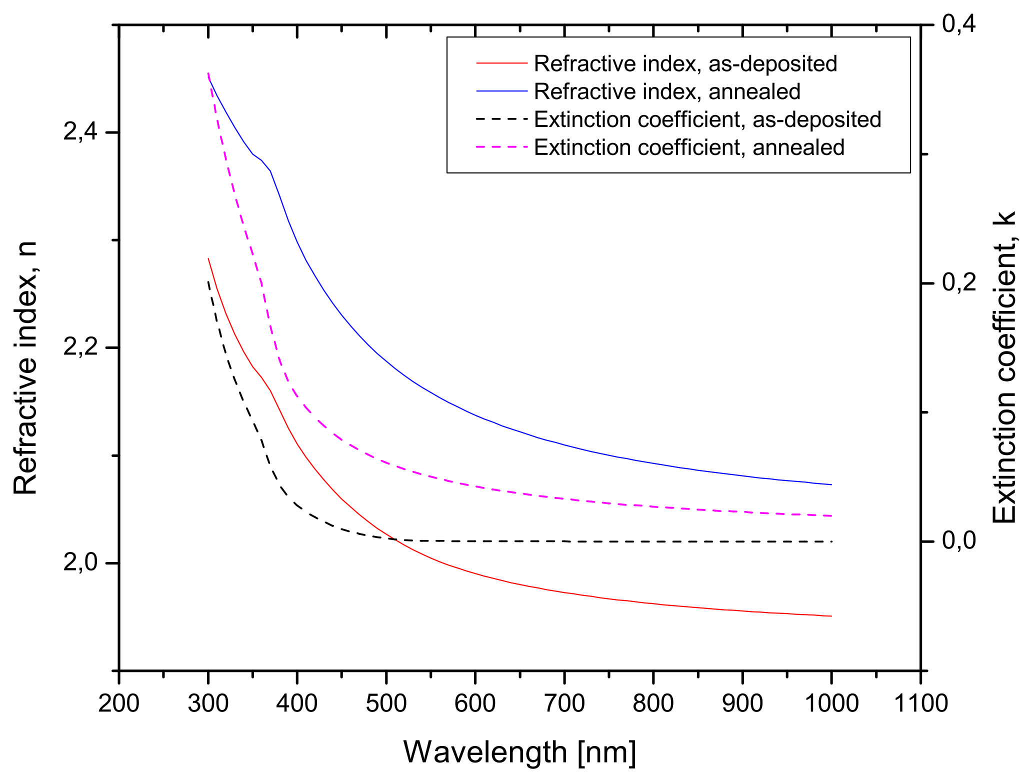

Figure 4.5: Optical constants for ammonia level of 31.2 sccm for annealed and as-deposited samples

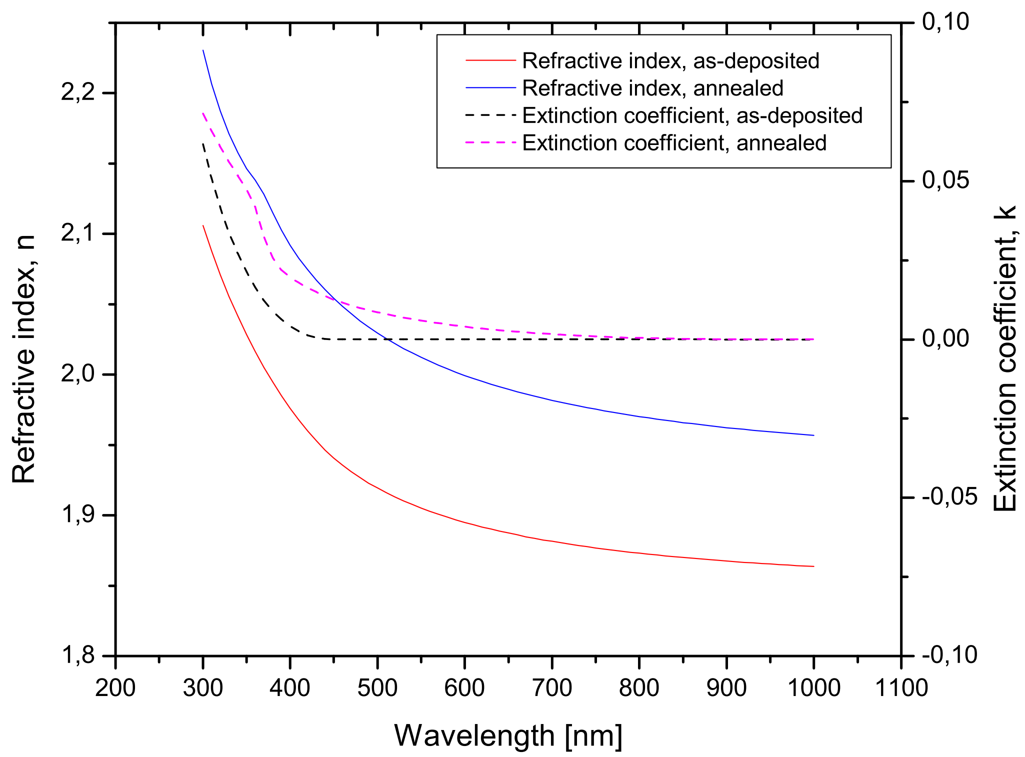

Figure 4.6: Optical constants for ammonia level of 50 sccm for annealed and as-deposited samples

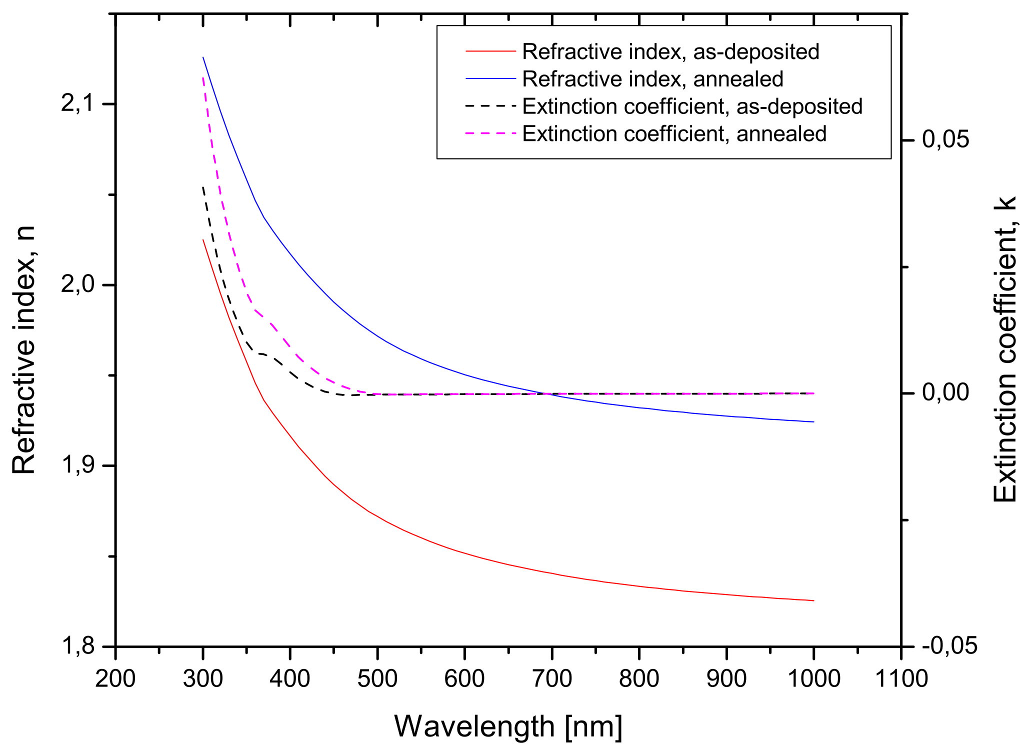

Figure 4.7: Optical constants for ammonia level of 50 sccm no H_2 for annealed and as-deposited samples

4.2 PL measurements

The room temperature PL measurements can be found in figures 4.8 and 4.9 for as-deposited and annealed samples respectively. The temperature dependent PL measurements for sample 7 both as-deposited and annealed can be found in figure 4.10. The PL measurements for both as-deposited and annealed samples 5, 6 and 7 at 10° K can be found in figure 4.11. The saturated PL spectrum for sample 7 in figure 4.11 is the saturated spectrum at room temperature. A higher sensitivity setup measurement for samples 1-4 can be found in figure 4.12. The main difference between the normal setup and the high sensitivity setup is that the high sensitivity setup has a broader dynamic range and is capable of detecting single photons. The high sensitivity measurements were carried out in room temperature.

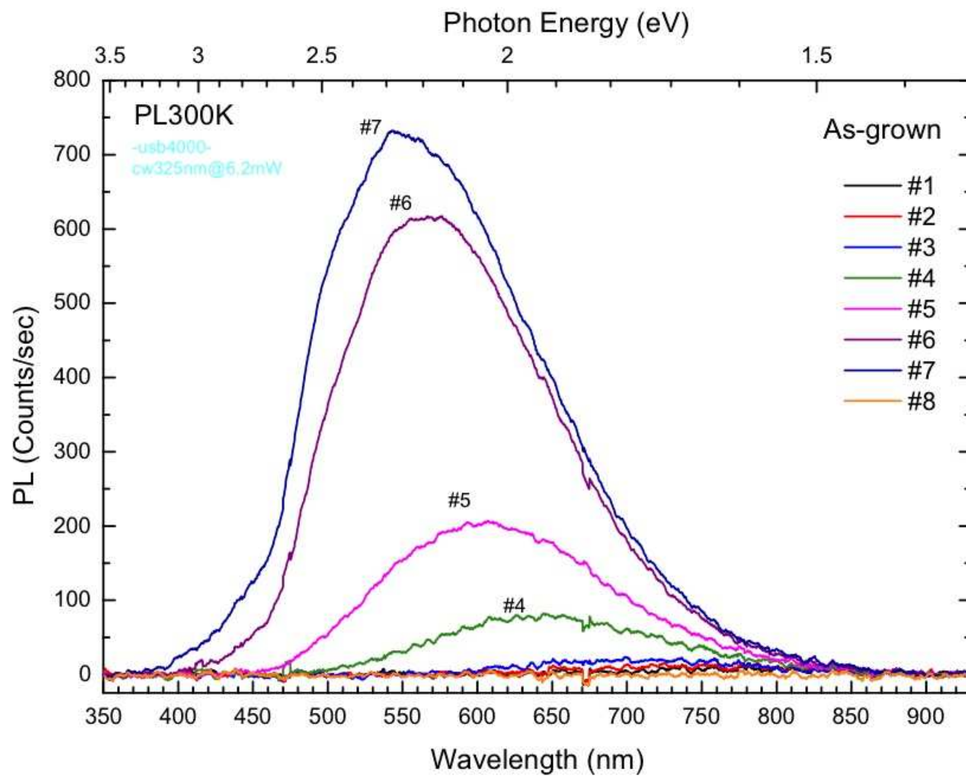

Figure 4.8: PL measurements at room temperature for as-deposited samples

The most obvious result based on the figures 4.8 and 4.9 is that samples

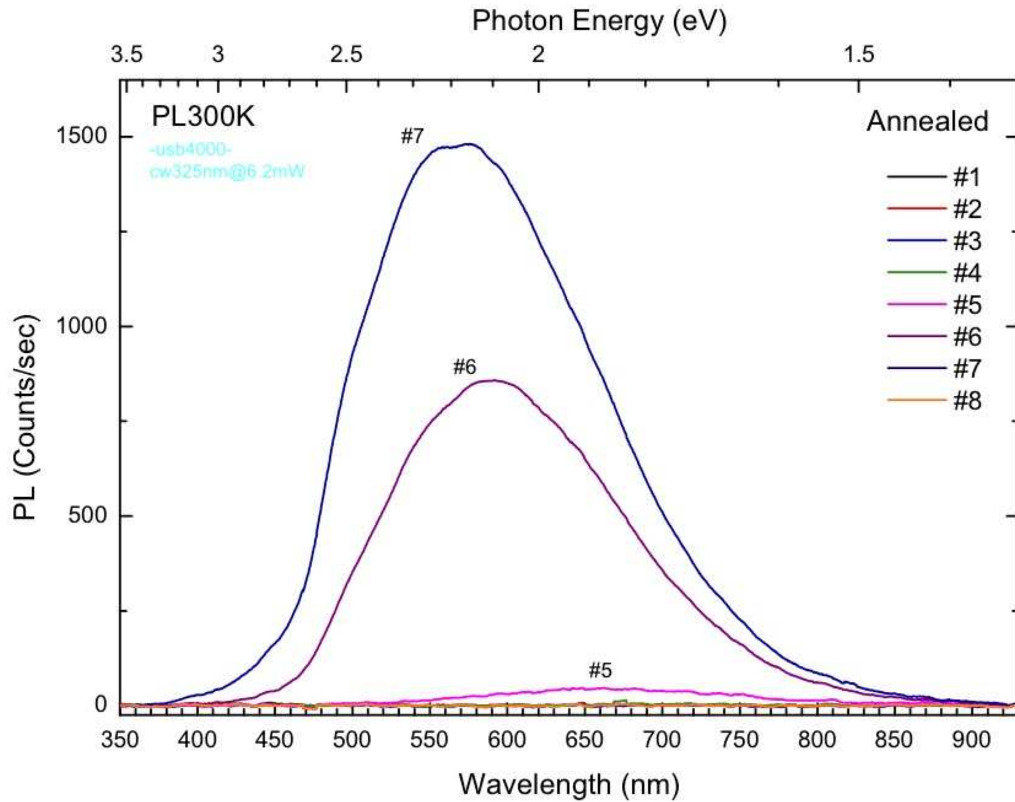

Figure 4.9: PL measurements at room temperature for annealed samples

1, 2, 3 and 4 yields very little luminescence. This is the reason for why only samples 5, 6 and 7 were selected for the temperature dependent PL measurements. Sample 8 is silicon substrate deposited with amorphous silicon (a-Si) and was included for reference. Table 4.7 shows the wavelengths for the PL peaks, the FWHM and the counts/sec at the peak for both as-deposited and annealed samples 5, 6 and 7. By looking at figure 4.10 it is clear that the peak position for the PL measurements changes little with changing temperature. The FWHM also changes little with temperatue (as is evident just by examining the graph). The only thing that is changing with temperature is the intensity, which is increasing with decreasing temperature. This result is found for both as-deposited and annealed samples. The graph in figure 4.11 shows how the as-deposited and annealed samples behaves at 10° K. For both sample 5 and 6 it is clear that there is a reduction in the PL intensity between annealed and as-deposited samples, for sample 7 the intensity is unchanged

between the annealed and as-deposited samples.

Table 4.7: Wavelength for PL peaks, FWHM and counts/sec

Sample #	Wavelength [nm]	FWHM [nm]	counts/sec
$5_{as-deposited}$	607	176	207
$6_{as-deposited}$	576	173	618
$7_{as-deposited}$	543	175	732
$5_{annealed}$	648	187	47
$6_{annealed}$	591	179	858
$7_{annealed}$	575	184	1482

By examining table 4.7 it is clear that the peak position for the PL changes with changing ammonia flow and before and after annealing. The peak position decreases in wavelength for increasing ammonia flow, and the count/sec increases with increasing ammonia flow. The FWHM changes little between the samples for both the as-deposited- and annealed ensemble. The peak position changes for all samples between the as-deposited and annealed ensemble, an increase in peak position is observed between the as-deposited ensemble and the annealed ensemble for all samples. The counts/sec increases for both sample 6 and 7, but is reduced for sample 5. So sample 6 and 7 seems to be following a trend when comparing the as-deposited an annealed ensembles, sample 5 does not.

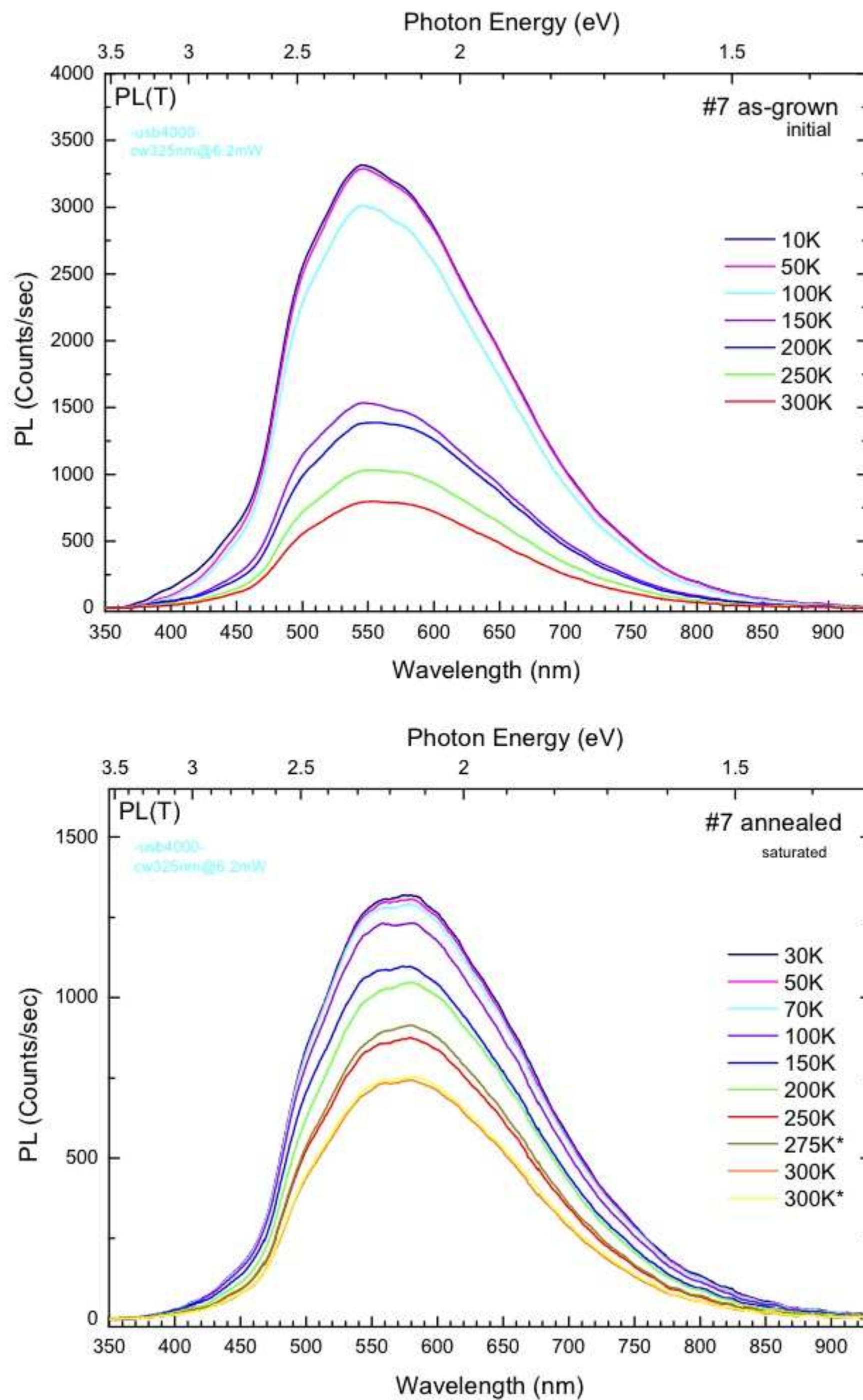

Figure 4.10: Temperature dependent PL measurements for as-deposited and annealed sample 7

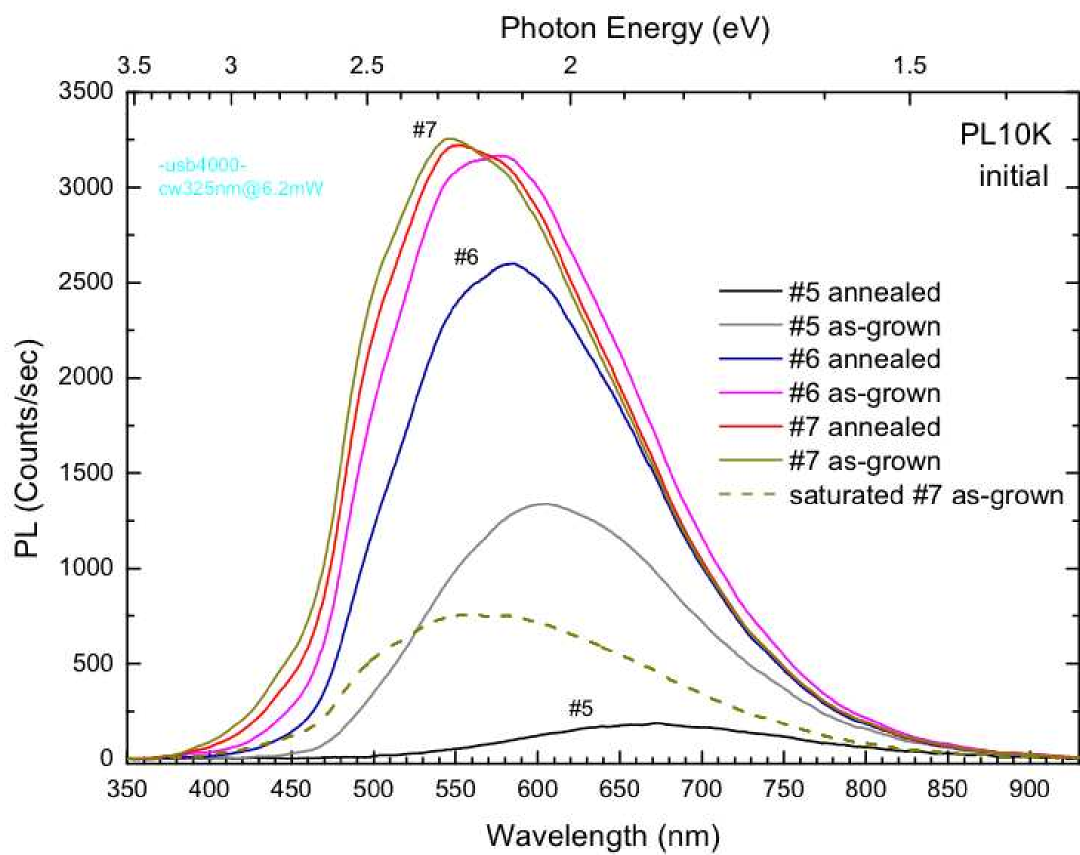

Figure 4.11: PL measurements for samples 5, 6 and 7 at 10° K

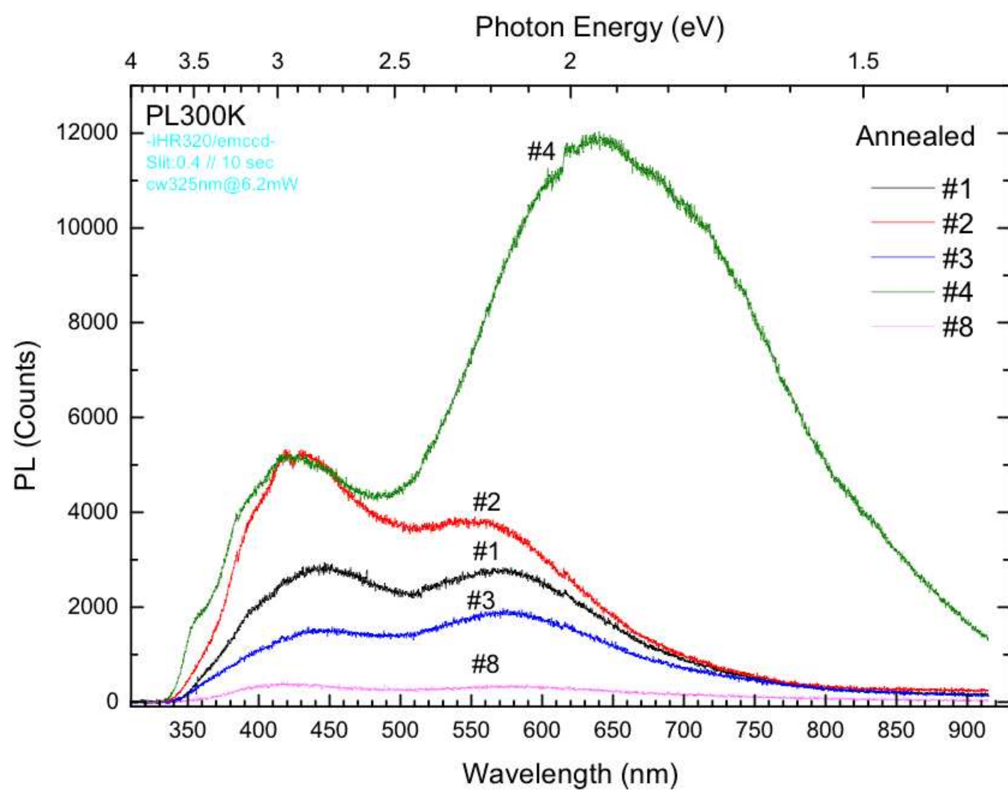

Figure 4.12: PL measurements for high sensitivity setup for samples 1-4

4.3 TEM results

Pictures from the TEM measurements can be found in images 4.13-4.19. Inspection of figures 4.13-4.16 reveals no presence of either silicon nanocrystals, or amorphous silicon nanoclusters. The dark clusters seen in images 4.17 and 4.18 are related to copper (Cu), that comes from the ion milling process. The TEM samples are glued to a Cu ring for stabilization. With a low angle on the Ar guns, Cu can sometimes be sputtered from the ring and be deposited on the sample. The dark nanoclusters should therefore not be confused with possible silicon nanostructures in the film. The last image, image 4.19 has two filtered images of sample 5. The filtering is related to the electron energy loss spectroscpy (EELS) spectrum. A major peak in this spectrum is related to the plasmon energy loss, the plasmon lose its energy to electrons in the valence band. The peak energy for this loss mechanism is found at 16.8 eV for silicon and 21 eV for silicon nitride. By applying a filter, the electrons that have lost the energy equal to the peaks can be imaged. By inspection of the image that has been filtered at 16 eV, it is possible to see amorphous clusters of silicon. The other samples were also filtered at 16 eV and 21 eV. No evidence of either amorphous silicon clusters or crystalline silicon nanoclusters were present, so these images have been left out.

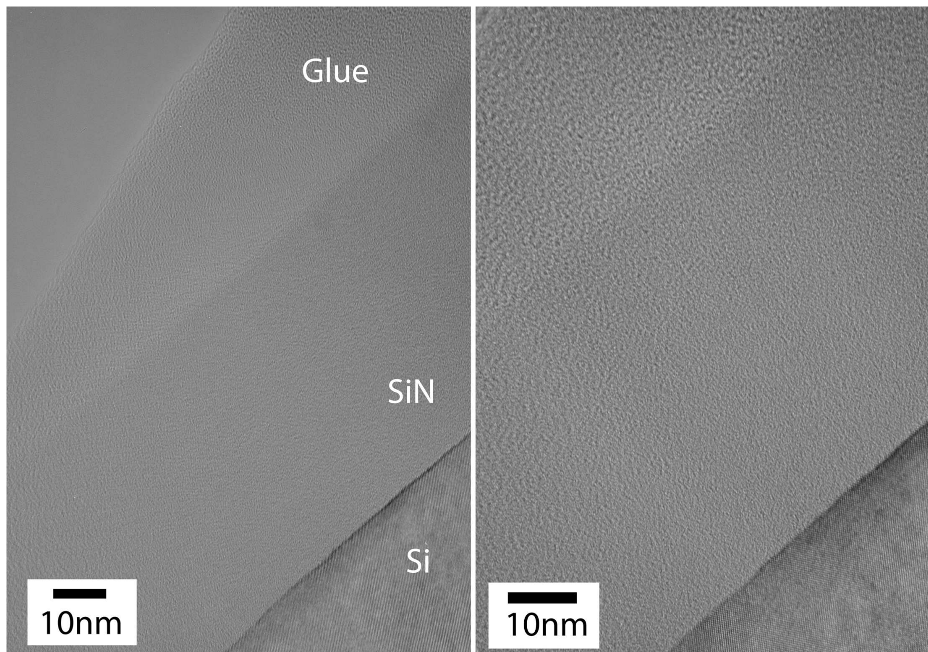

Figure 4.13: TEM image of annealed sample 4

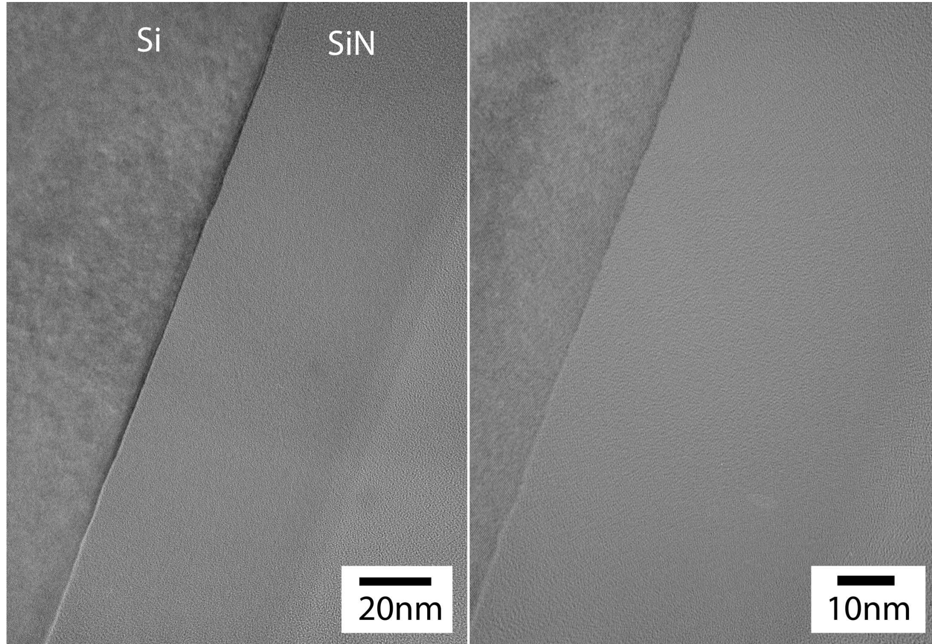

Figure 4.14: TEM image of annealed sample 5

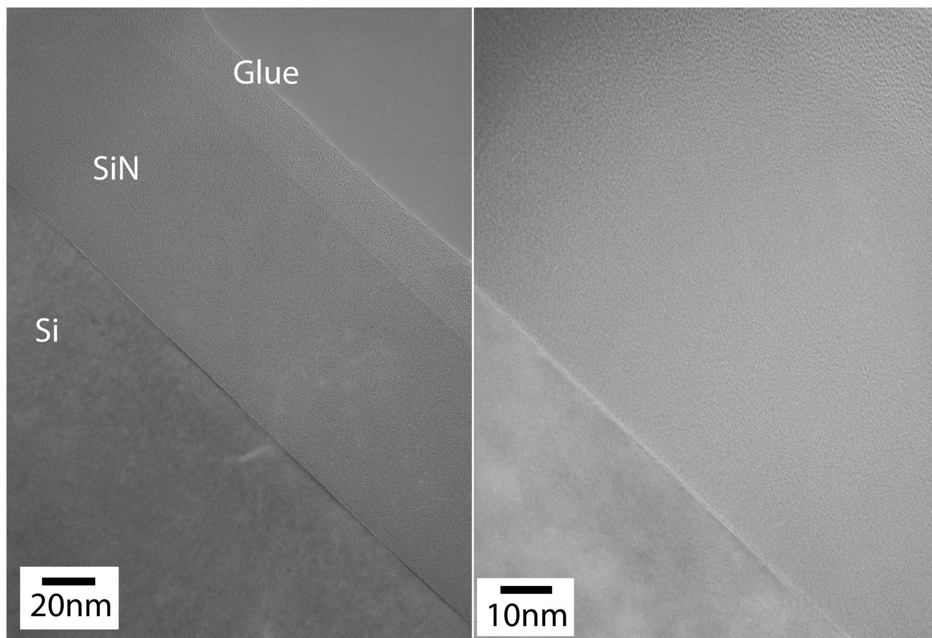

Figure 4.15: TEM image of annealed sample 6

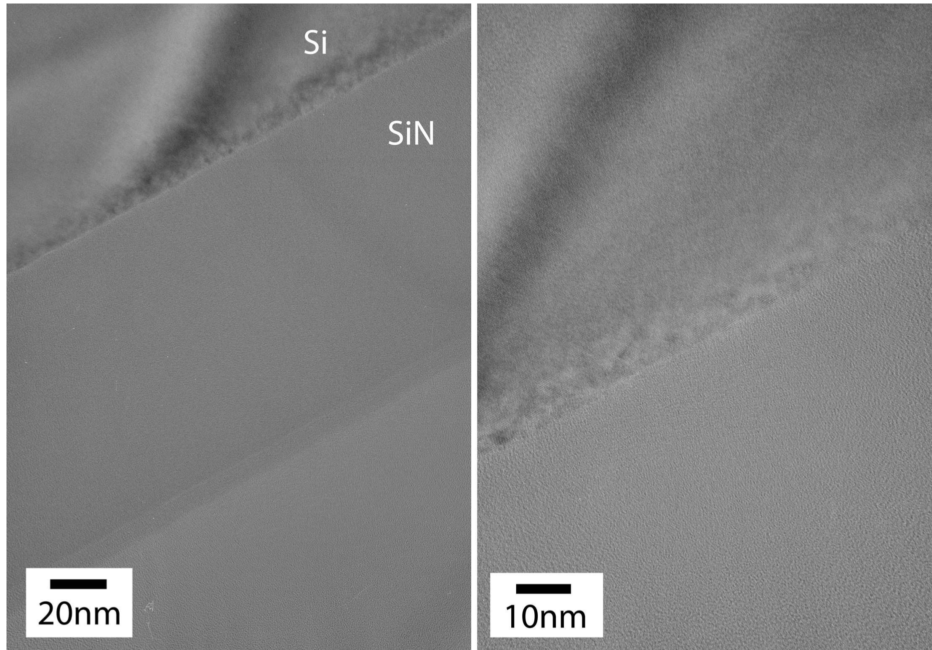

Figure 4.16: TEM image of annealed sample 7

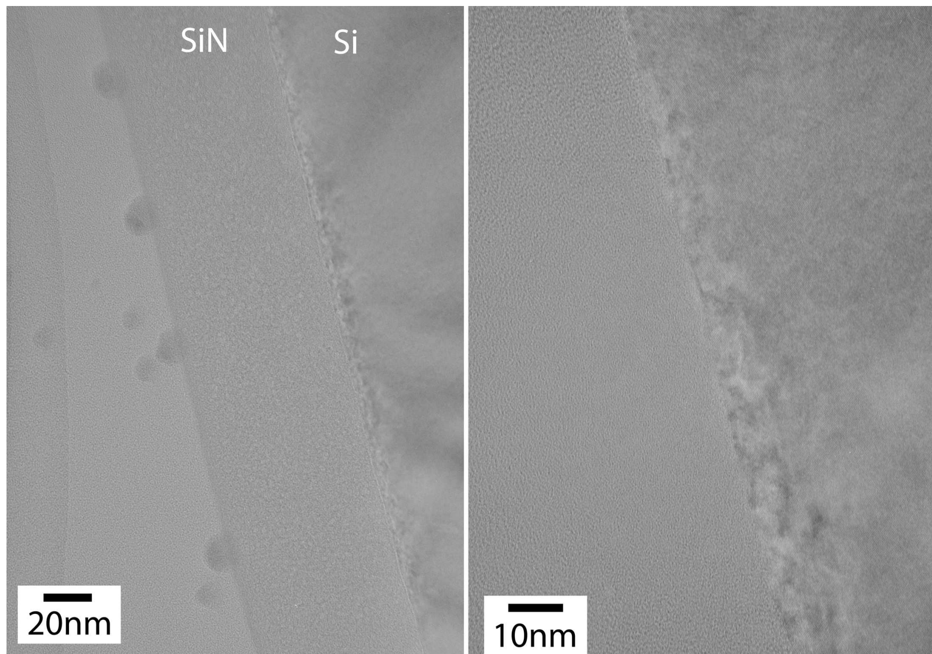

Figure 4.17: TEM image of as-deposited sample 5

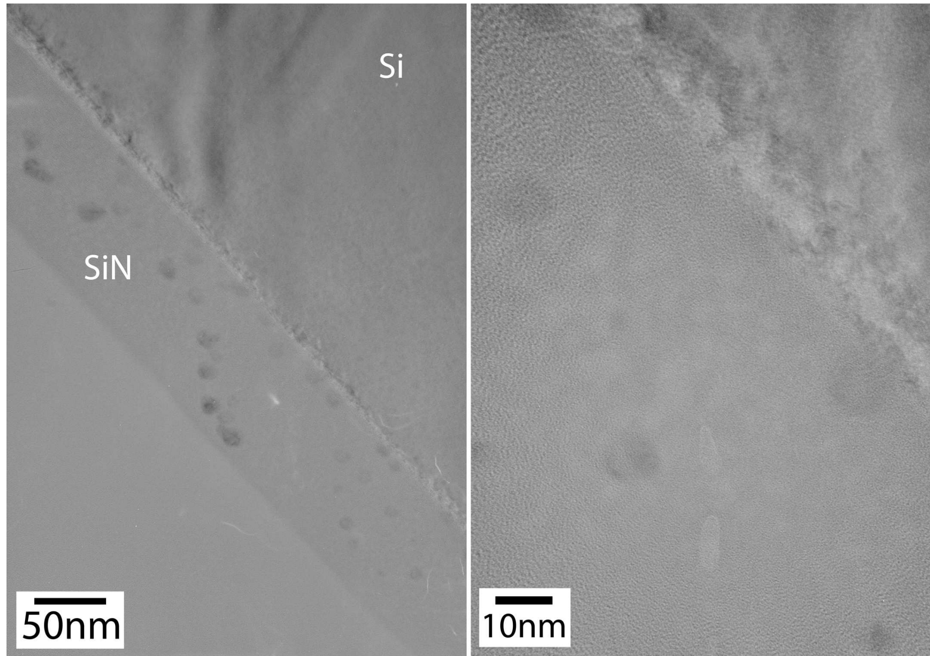

Figure 4.18: TEM image of as-deposited sample 6

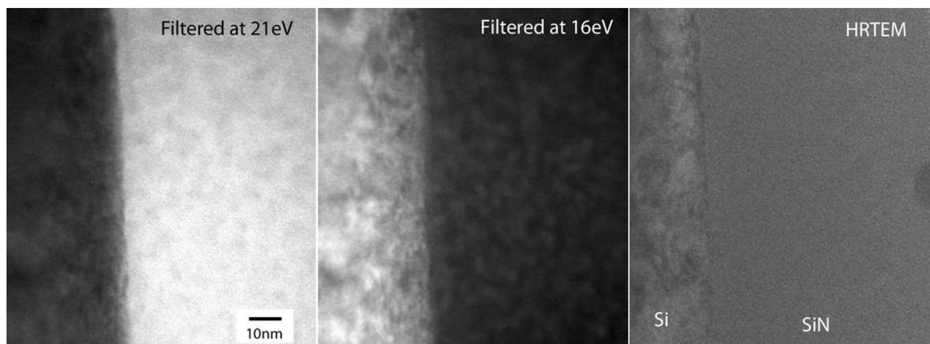

Figure 4.19: TEM image of as-deposited sample 5, filtered at 21 and 16 eV

CHAPTER 5

Discussion

The results found in chapter 4 will be discussed in the order as they appear in the chapter.

5.1 Ellipsometry

There are several aspects of the model found for the ellipsometer data that needs to be commented on. These are the fact that the model is unable to follow kinks in the experimental data and the fact that the weighing of each of the constituents in the BEMA model seems to be random between the consecutive samples in the as-deposited ensemble, as well as the annealed ensemble. The change in the weighing of the constituents of each of the samples before and after annealing also seems to be random. Ideally one would hope that there would be a trend developing between consecutive samples and also between each sample before and after annealing. What might look like the most surprising result is the fact that the thickness is changing between the as-deposited and annealed ensembles could very well be a physical result. It is stated in an article by *Ma et al*, [34] that hydrogen disorption can occur for samples that are annealed, this and the fact that the film get more compact because of the annealing could yield films that are thinner as a result of the annealing process (ta med siteringer på det kanskje). Another obvious point to make about the thickness is that it changes between individual samples in the two ensembles. This might be explained by the fact that each of the samples undergoes an individual process when the film is deposited. Some

of the process parameters that ideally should be kept constant (everything except for the ammonia flow) may not remain constant, so this could possibly affect the thickness of the individual samples. Another reason for why the film thickness is different for individual samples could be explained by the fact that the ammonia level is increasing for successive samples. As the ammonia level increases, the quantity of material arriving at the growing film also increases. This could very well be one of the reasons for why the film thickness is also increasing for successive samples as is evident by examining tables 4.3 and 4.4, (the increase is observed for all successive samples, except for samples 2 and 3 were a decrease is observed for both the as-deposited and annealed ensembles). The increase in film thickness was also observed in [26], were an increase in the ammonia level gave thicker films. The increase in film thickness was attributed to the increase in ammonia level. One way of eliminating the thickness as a fit parameter could be to perform a topographic measurement by atomic force microscopy (AFM), other ways could be by TEM or profilometry.

It seems like the film is not stoichiometric nitride because there are several examples where stoichiometric nitride films with different thickness have been fitted with a Tauc-Lorentz ocsillator and the model fits the measured data extremely well, [25], [23] and [11]. As stated in section 3.3 stoichiometric nitride was used as a starting point for the T-L oscillator, but when the T-L oscillator fitted for the stoichiometric nitride was applied to the samples, it did not yield a satisfying result, so the model was expanded with a BEMA layer. Also stated in article [11] where Si-rich nitride films are analyzed with an ellipsometer it is stated that the bandgap (E_g) in the T-L model should decrease with increasing silicon to nitrogen ratio (this is also stated in [15] and [49]), when looking at tables 4.1 and 4.2 this is clearly not the case. This does not mean that the results obtained are non-physical. The T-L oscillator is one of three materials that the BEMA model is comprised of. In order to fit the measured data in the best possible way it could be that the given value for the band-gap together with the weighing of the other two constituents is what fits the measured data best. This argument can also be used to explain why the weighing of voids seems to be increasing for some samples after annealing. Annealing is known for removing voids and defects from the film, [5], so one might intuitively expect to see a reduction in the weighing of voids. But again, combined with the T-L oscillator and crystalline silicon, this might be what fits the measured data best. By examinig tables B.1 and B.2 it is clear that the final values of the band-gap is closer to following the trend that an increase in the ammonia level should yield a higher band-gap as described in [11], [15] and [49]. This could mean that

by changing the crystalline silicon in the BEMA model with silicon nitride, the T-L oscillator is more closely descrbing the silicon in the silicon nitride instead of describing a film with excess silicon and voids.

It has been stated in [23] that parts of the spectrum where the fit seems to be poor could be because of peaks in the real part of the reflection coefficient or discontinuities in the imaginary part of the reflection coefficient. A major problem when trying to find a good model for the ellipsometry measurements is that the deposited film could be (or probably is) comprised of several sublayers. Good agreement between the model and the ellipsometry measurments have been found in [16] where the film was divided into 5 sublayers. The deposition conditions were not the same as in this experiment though. The precursor gases were H_2, SiH_4 and TMB (Trimethylboron). It is very interesting to see how the fraction of amorphous silicon, nanocrystalline silicon and voids changes between successive sublayers. Good results between the modelled and experimental data were also obtained in [7], in this experiment the film was divided into 15 sublayers, each layer was then modelled with a BEMA layer. As stated in section 3.3 to get a good fit for the model the starting point needs to be relatively close to the actual film, so if one wants to divide the film into several sublayers, more information is definitely needed in order to make a good "qualified guess". In concluding remarks a more refined model that is able to describe specific parts of the film in a better way should be a goal to aim for. If there are silicon nanocrystals present in the film it would be preferable if the T-L oscillator describe these as the T-L oscillator can reveal some interesting physical aspects of the nanocrystals (the band-gap energy possibly being the most interesting parameter).

The last thing to comment on is the refractive index and the extinction coefficient for the samples. Figures 5.1 and 5.2 give the refractive index and extinction coefficient for crystalline silicon and stoichiometric silicon nitride respectively. The reference for silicon can be found in [41], while the reference for silicon nitride can be found in [20]. It is evident that the shape of the refractive index of samples 1, 2 and 3 resembles that of silicon (ref. fig. 4.1-4.3), but that the index is lower for the samples compared to that of silicon. The lower index of refraction is also an indication of the *porous*[1] nature of the films as stated in [47]. The increase in the refractive index after annealing as is observed for all samples is an indication that the films

[1]Porosity is a measure of the void spaces in a material, and is a fraction of the volume of voids over the total volume.

have become more compact. As the ammonia level is increased, the shape of the index of refraction changes, the shape now resembles that of silicon nitride. The refractive index is also closer to that of silicon nitride. This is not suprising as one should expect the refractive index of the film to resemble that of stoichiometric nitride when the ammonia level is increased, because there is less excess silicon in the film. An interesting point to notice is that the MSE is generally lower for samples 4, 5 and 6 (except for the as-deposited sample 6) when crystalline silicon is exchanged with silicon nitride in the BEMA model (ref tables 4.3, 4.4, B.3 and B.4). This could mean that as the ammonia level is increasing, the BEMA model containing silicon nitride instead of crystalline silicon can better describe the measured data. By comparing the plot of the optical constants in each of the two cases it is also clear that the shape of the refractive index resembles that of silicon for both samples 4 and 5 for the latter case, for the first case the shape resembles that of silicon nitride. This could be attributed to the T-L oscillator, now describing the behaviour of silicon (in a silicon nitride matrix), this can also be supported by the trend seen in the value of the energy-gap (an increase in energy-gap with decreasing excess silicon, ref. tables B.1 and B.2). Also the overall values of the refractive indices for all samples is in good agreement with values found in [30] where silicon nanocrystals were created within a silicon nitride matrix.

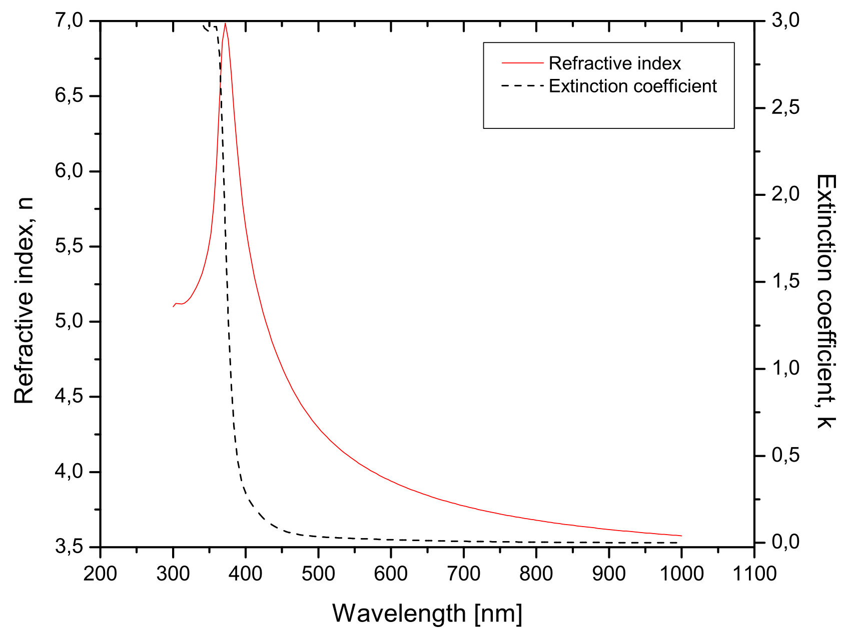

Figure 5.1: Optical constants for silicon

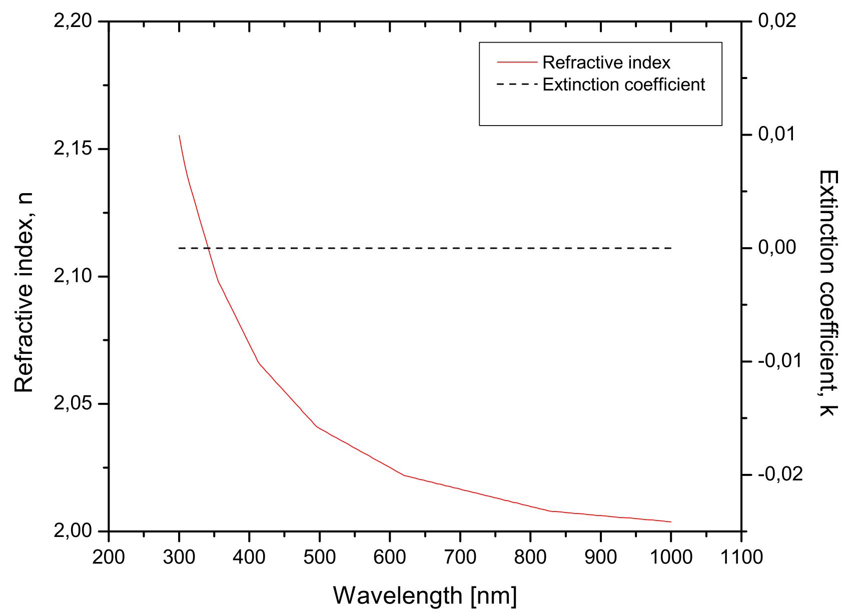

Figure 5.2: Optical constants for silicon nitride

5.2 PL measurements

Understanding the source(s) of luminescence (or the lack of luminescence for that matter) is very difficult, this is because there are several sources that can contribute to luminescence, and distinguishing one from another is very challenging. The main possible sources for luminescence in this experiment are the silicon nitride matrix itself, defects within the film, interface states between the silicon matrix and the silicon nanocrystals/excess silicon, the silicon nanocrystals/amorphous silicon nanoclusters (if present) and interface states between the silicon nitride matrix and the substrate. Raman scattering spectroscopy and density functional theroy (DFT) calculations are two methods that can help in characterizing the bonding structure of the film, this was done in for example [38] but was not done in this experiment. Based on the results from the PL measurements at room temperature only sample 5, 6 and 7 were selected for temperature dependent PL measurements. This was justified by their large peaks compared to the remaining samples at wavelengths of around 570-610 nm. According to an article written by *Wang et al.*, [54], the peak seen at the wavelengths given in table 4.7 is attributed to silicon- or nitrogen dangling bond centers. The deposition conditions in [54] were similiar to this experiment. The films were deposited with the PECVD method with a substrate temperature of 300° C. The precursor gases were NH_3 and N_2 diluted SiH_4. The $\frac{NH_3}{SiH_4}$ ratio was varied between 1 and 10. When the samples in this experiment were excited by the 325 nm excitation source, peaks that are similar to the peaks in this experiment show up. There is one additional peak at around 400 nm, this was attributed to nitrogen dangling bonds. This peak is not seen for samples in this experiment, this could be because of the lack of a pure nitrogen source. Also in articel [54] another excitation source operating at 514.5 nm is used to investigate the PL in the infrared, this gives PL peaks at 640-720 nm for three different samples. This peak is attributed to the silicon nanoclusters. A red shift is observed, this shift is attributed to the increasing size of the nanoclusters. Now looking at the main peaks (ref. table 4.7) it might be that there are silicon nanoclusters present in the film, but due to the broad peak it might not be possible to detect them (the FWHM extends from 489.5 to 662.5 nm and 455.5 to 630.5 for sample 6 and 7 respectively). Inspection of figure 4.12 reveals a peak for sample 4 at around 650 nm, a peak at around the same wavelength was observed in article [54] and this was attributed to silicon nanoclusters.

An article written by *Kim et al.*, [27] specifically relates PL peaks at 1.8, 2.4 and 3 eV to defects. The peak at 1.8 eV is related to the recombination between N_4^+ and N_2^0, while the peak at 2.4 eV is related to the recombi-

nation in the silicon dangling bonds and the 3 eV is due to recombination either from the conduction band to the N_2^0 level or from the valence band to the N_4^+ level, [14]. The samples in article [27] did not have any specific PL peaks at the corresponding energy levels, and the position of the PL peak was controlled by varying the levels of the precursor gases. The change in position for the PL peaks depending on the ratio of the precursor gases are also observed for samples that have a detectable PL at room temperature (ref. figures 4.8 and 4.9) in this experiment. The effect of changing either the SiH_4 flow or the NH_3 is also commented on in article [27], and it is concluded that an increase in the SiH_4 flow while keeping the NH_3 flow constant induce a red shift in the PL peak, while an increase in the NH_3 flow while keeping the SiH_4 constant induce a blue shift in the PL peak, this has also been concluded in [42][2]. In article [27], it is also stated that the increase in the NH_3 level appears to promote dissociation of Si-H bonds and that this increases the number of silicon dangling bonds. The silicon dangling bonds may then facilitate creation of nucleation sites. This has also been confirmed in [28] and [42]. In an articel written by *Dal Negro et al.* [39] the observed photo-luminescence is attributed to the different Si-N bonding groups that is passivating the interface between the Si clusters and the matrix. This was based on the lack of tunability observed when the stoichiometry of the film was changed, and the fact that the temperature dependent PL spectra can be described by the formula:

$$I_{PL}(T) = I(0)\{1/[1 + \beta \exp(-E_A/k_B T)]\} \tag{5.1}$$

where $I(0)$ is the PL intensity at the lowest measured temperature, β is a constant that is inversely proportional to the radiative rate of the system and E_A is an activation barrier. This result was also confirmed in [37] and can be directly related to the temperature dependent PL results obtained for sample 7 which is following the behaviour described by equation 5.1 with $E_A = 32$ meV. The lack of photoluminescence that is observed for the as-deposited samples 1-3 and for the annealed samples 1-4 could possibly be related to hydrogen desorption as stated in [34]. Also the annealing temperature of 1050° C might be too high, it has for example been stated in [37] that a maximum in PL intensity was reached for an annealing temperature of 700° C for 10 min. For temperatures above this, a decrease in PL intensity is observed. A similar result can also be found in an article written by *Tarasov et al.*, [52], a maximum in the PL intensity is detected for an annealing temperature of 740° C. For annealing temperatures above this, a reduction in PL intensity is observed. It is believed that the reduction in PL is caused by

[2] In this experiment N_2 was used as a precursor gas instead of NH_3

the out-diffusion of hydrogen, which lead to a reduction in the passivating effect. In an article written by *Benami et al.*, [2] it is stated that samples that are deposited with a flow rate of ammonia of 10 sccm and below yields little or no PL.[3] This is also what is observed for the samples with the lowest ammonia flow in this experiment (samples 1-3 in the as-deposited ensemble and samples 1-4 for the annealed ensemble). The low ammonia flow leads to more excess silicon in the film, and it is possible that unpassivated silicon dangling bonds serves as non-radiative recombination centers. The high annealing temperature together with the desorption of hydrogen might explain why sample 4 that has some PL for the as-deposited case has no PL for the annealed case. The same reasoning might explain the reduced PL seen for sample 5 between the as-deposited and annealed ensembles.

The formula below is typically given [27, 42] to show the correlation between the PL peaks and the energy gap for silicon nanostructures:

$$E(eV) = E_{bulk} + C/d^2 \tag{5.2}$$

where E_{bulk} is the band-gap of bulk silicon, d is the size of the silicon nanostructure and C is a confinement parameter. In [42] the values that fitted the data best was $E_{bulk} = 1.56$ and $C = 2.40$, while in [27] the values were equal to 1.16 and 11.8 for E_{bulk} and C respectively. The first case represents amorphous silicon nanoclusters, while the latter represents crystalline nc-Si. Applying formula 5.2 to the PL results obtained for sample 4 with the high sensitivity setup gives values of $d = 3.86$ nm and 2.48 nm for the crystalline and amorphous case respectively. It is worth pointing out that amorphous silicon clusters with the size calculated, if present in the film, will be hard to detect by TEM. Also by examining tables 4.1 and 4.2 it is clear that the values given for the energy gap would yield negative values for the size of the amorphous clusters if applied to equation 5.2. This is clearly a non-physical result and serves as an indicaton that the energy gaps are not directly related to any silicon clusters (present or non present).

To summarize the results; no solid conclusion can be made as to pinpoint the exact sources of the observed luminescence. Both defect related/interface states and nanocrystals have been mentioned as possible sources for luminescence. Based on the PL measurements obtained and the uncertainty regarding the sources of the luminescence, no conclusion can be made as to whether there are silicon nanocrystals present in the film or not.

[3] $SiCl_4$ was used as a precursion gas instead of SiH_4, the $SiCl_4$/H2 ratio was kept constant at 0.25

5.3 TEM images

Based on the images shown in section 4.3, no evidence of any nanostructures is observed, the only exception being the as-deposited sample 5 were amorphous silicon clusters are seen. The lack of observed nanostructures gives support to one of the conlusions reached in article [54] were the main PL peaks seen at around 570-610 nm are attributed to silicon or nitrogen dangling bond centers. The result also supports a similar conclusion reached in article [39]. Another conlusion that was reached in [54] was that the peaks seen at around 640-720 nm were related to silicon nanoclusters, a peak at around 650 nm is seen for the annealed sample 4, but no nanoclusters were observed with TEM (this includes filtering at 16 and 21 eV), this could mean that the observed peak is related to defect or interface states. As for the tunability of the peak postion that was commented on in [27, 42] and related to silicon nanoclusters, no such conclusion can be made with the given TEM images since there are no evidence of any nanoclusters present in the film.

The film thickness obatined from the TEM images can be found in table 5.1, the corresponding thickness found with the ellipsometry model from section 3.3 is also included together with the ratio in thickness found with TEM and ellipsometry measurements.

Table 5.1: Thickness found with both TEM and the ellipsometry model from section 3.3 for selected samples

Sample #	thickness TEM [nm]	thickness ellipsometry [nm]	Ratio [%]
$4_{annealed}$	53	56	5
$5_{as-deposited}$	68	76	11
$5_{annealed}$	63	72	13
$6_{as-deposited}$	89	102	12
$6_{annealed}$	77	90	14
$7_{annealed}$	107	127	16

Another comparison between the thickness found with the BEMA model described in appendix B and the thickness found with TEM can be found in table 5.2

It is worth pointing out that the relative change between the TEM thickness and the thickness found with the ellipsometry model is smaller for all samples except for sample 1 when the BEMA model from appendix B is used. This and the lower MSE found for the model in appendix B indicates that this model is a better fit when ammonia to silane ratio is greater than 1.

Table 5.2: Thickness found with both TEM and the ellipsometry model from appendix B for selected samples

Sample #	thickness TEM [nm]	thickness ellipsometry [nm]	Ratio [%]
$4_{annealed}$	53	44	20
$5_{as-deposited}$	68	73	7
$5_{annealed}$	63	65	3
$6_{as-deposited}$	89	100	11
$6_{annealed}$	77	87	11

CHAPTER 6

Conclusion and further work

This work has focused on different techniques that are used to analyze anti-reflective coatings used in the solar cell industry. The initial aim was to get films that also contained nanostructures, either in the form of nano-crystalline silicon or amorphous silicon clusters. Although only one sample (sample 5) returned promising results with respect to finding any silicon nanostructures, this report has highlighted several aspects of the techniques used to analyze thin film anti-reflective coatings. The task of analyzing the films ultimatley gets more complex when one also wants to verify the presense of silicon nanostructures in the films.

The two ellipsometry models presented in the report are almost identical except that one of the constituents in the BEMA layer is substituted with a different material. Based on the MSE obtained and the thickness found with TEM it is clear that witht the changing ratio of ammonia to silane flow, one of the two models will more accurately describe the film than the other. The model found in section 3.3 is better than the model found in appendix B when the ratio of ammonia to silane is less than 1. When this ratio becomes greater than 1, it is the other way round. The optical constants found with both models also highlight the porosity of the deposited films. One of the effects of annealing is also observed for all samples in both models, and that is the increase in optical constants. This is because the films get more compact due to the annealing process. An interesting observation is made for the thickness of the as-deposited and annealed sample 5. The relative ratio in thickness obtained with the ellipsometry model in section 3.3 gives a ratio

of 5%, the thickness obtained with TEM gives a ratio of 7%. This differs from the other samples were the relative change is around 11%. It is possible that the observed silicon nanoclusters give a more rigid film that results in a smaller relative change in thickness due to the annealing process.

The PL measurements yielded several interesting results, but it proved hard to point at the exact sources of the luminescence, this is also seen in the litterature. As no evidence of any nanoparticles was found for samples 6 and 7 it seems likely that the observed PL peaks are related to defect states in the film. The most surprising result was that no evidence of any nanostructures was found for the annealed sample 4, which has a very characteristic PL peak at around 650 nm. The only sample with any evidence of nanostructures was the as-deposited sample 5, which had amorphous silicon clusters. The PL peak related to the sample was broad (FWHM=187nm) and most likely related to defect states, so any contributions from the nanoclusters would be hard to detect. The low PL signals observed for samples 1,2 and 3 is likely related to unpassivated defect states, the further reduction in PL observed for the annealed samples 1-5 is related to the desorption of hydrogen.

The two main areas to focus on for possible future work would be a more refined ellipsometry model that can closer describe the different constituents of the films and how they change with position in the film. The introduction of sublayers have been mentioned in the litterature and seems like a logic next step for the model. Also, a different starting point for the T-L oscillator seems interesting. The T-L oscillator was fitted to stoichiometric nitride for this experiment. It would be interesting to use crystalline silicon as the material to which the T-L oscillator is fitted to, the reason being that the T-L oscillator might be more capable of describing silicon nanostrcutures, if present. Fourier transform infrared spectroscopy (FTIR) seems like an obvious candidate for the characterization of the composition of the film. A more refined ellipsometry model may then be built on the basis of the results obtained with FTIR and the thickness obtained with TEM. Another way of characterising the bonding structure is the Raman scattering spectroscopy.

The second point to focus on is the annealing process. The effect of both annealing time and annealing temperature is not fully understood. The as-deposited samples should be treated in a range of temperatures, for example a range between $600^\circ - 1000^\circ$ C. Ellipsometry measurments, PL measurements and TEM should be performed on the anneald samples in order to observe the changes/effects that the different annealing temperatures have on the films.

Bibliography

[1] D. E. Aspnes. Optical properties of thin films. *Thin Solid Films*, 89, 1982.

[2] A Benami, G Santana, A Ortiz, A Ponce, D Romeu, J. Aguilar-Hernandez, G. Contreras-Puente, and J C Alonso. Strong white and blue photoluminescence from silicon nanocrystals in SiN_x grown by remote PECVD using $SiCl_4/NH_3$. *Nanotechnology*, 18, February 2007.

[3] D. A. G. Bruggeman. Berechnung verschiedener physikalischer konstanten von heterogenen substanzen. i. dielektrizitätskonstanten und leitfähigkeiten der mischkörper aus isotropen substanzen. *Annalen der Physik*, 416:636–664, 1935.

[4] L. Cai, A. Rohatgi, D. Yang, and M. A. El-Sayed. Effects of rapid thermal anneal on refractive index and hydrogen content of plasma enhanched chemical vapor deposited silicon nitride films. *Journal of Applied Physics*, 80, August 1996.

[5] Stephen A. Campbell. *Fabrication Engineering at the micro- and nanoscale*. Oxford University Press, New York, New York, 2008.

[6] L. T. Canham. Silicon quantum wire array fabrication by electrochemical and chemical dissolution of wafers. *Applied Physics Letters*, 57, September 1990.

[7] Z. H. Cen, T. P. Chen, L. Ding, Y. Liu, M. Yang, J. I. Wong, Z. Liu, Y. C. Liu, and S. Fung. Annealing effect on the optical properties of

implanted silicon in a silicon nitride matrix. *Applied Physics Letters*, 93, July 2008.

[8] James R. Chelikowsky and Marvin L. Cohen. Electronic structure of silicon. *Physical Review B*, 10:5095–5107, December 1974.

[9] Eun-Chel Cho, Martin A. Green, James Xia, Richard Corkish, Peter Reece, and Mike Gal. Clear quantum-confined luminescence from crystalline silicon/SiO_2 single quantum wells. *Applied Physics Letters*, 84, March 2004.

[10] J. W. Christian. *The Theory of Transformations in Metals and Alloys (Part I+II).* Pergamon, Oxford, UK, 2002.

[11] Candi S. Cook, Terry Daly, Ran Liu, Michael Canonico, Q. Xie, R. B. Gregory, and Stefan Zollner. Spectroscopic ellipsometry for in-line monitoring of silicon nitrides. *Thin Solid Films*, pages 794–797, 2004.

[12] A. G. Cullis and L. T. Canham. Visible light emission due to quantum size effects in highly porous crystalline silicon. *Nature*, 353, September 1991.

[13] B. Delley and E. F. Steigmeier. Quantum confinement in si nanocrystals. *Physical Review B*, 47, September 1992.

[14] Sadanand V. Deshpande, Erdogan Gulari, Steven W. Brown, and Stephen C. Rand. Optical properties of silicon nitride films deposited by hot filament chemical vapor deposition. *Journal of Applied Physics*, 77:6534–6541, June 1995.

[15] Alain C. Diebold. *Handbook of silicon semiconductor metrology.* Marcel Dekker, Inc., 270 Madison Avenue, New York, NY, USA, 2001.

[16] S. A. Filonovich, H. Aguas, I. Bernacka-Wojcik, C. Gaspar, M. Vilarigues, L. B. Silva, E. Fortunato, and R. Martins. Highly conductive p-type nanocrystalline silicon films deposited by rf-pecvd using silane and trimethylboron mixtures at high pressure. *Elsevier: Vacuum*, 83:1253–1256, 2009.

[17] Martin A. Green. Silicon solar cells: evolution, high-efficiency design and efficiency enhancements. *Semiconductor Science Technology*, 8:1–12, 1993.

[18] Martin A. Green. *Third Generation Photovoltaics Advanced Solar Energy Conversion.* Springer-Verlag, Berlin, Germany, 2003.

[19] Martin A. Green, Keith Emery, Yoshihiro Hishikawa, and Wilhelm Warta. Solar cell efficiency tables (version 33). *Progress in photovoltaics: Research and applications*, 17:85–94, 2009.

[20] C. M. Herzinger, B. Johs, W. A. McGahan, and J. A. Woollam. Ellipsometric determination of optical constants for silicon and thermally grown silicon dioxide via a multi-sample, multi-wavelength multi-angle investigation. *Journal of Applied Physics*, 83:3323–3336, November 1997.

[21] Fabio Iacona, Giorgia Franzo, and Corrado Spinella. Correlation between luminescence and structural properties of si nanocrystals. *Journal of Applied Physics*, 87, February 1999.

[22] IEA. 30 key energy trends in the iea & worldwide. 2005.

[23] G. E. Jellison, V.I. Merkulov, A. A. Puretzky, D. B. Geohegan, G. Eres, and D. H. Lowndes. Characterization of thin-film amorphous semiconductors using spectroscopic ellipsometry. *ICMCTF*, 2000.

[24] G. E. Jellison and F. A. Modine. Parameterization of the optical functions of amorphous materials in the interband region. *Applied Physics Letter*, 69:371–373, July 1996.

[25] G. E. Jellison, F. A. Modine, P. Doshi, and A. Rohatgi. Spectroscopic ellipsometry characterization of thin-film silicon nitride. *Thin Solid Films*, pages 193–197, 1998.

[26] A.-S. Keita, A. En Naciri, F. Delachat, M. Carrada, G. Ferblantier, and A. Slaoui. Spectroscopic ellipsometry investigation of the optical properties of nanostructured Si/SiN_x films. *Journal of Applied Physics*, 107, May 2010.

[27] Baek-Hyun Kim, Chang-Hee Cho, Tae-Wook Kim, Nae-Man Park, Gun Yong Sung, and Seong-Ju Park. Photoluminescence of silicon quantum dots in silicon nitride grown by NH_3 and SiH_4. *Applied Physics Letters*, 86, February 2005.

[28] Tae-Youb Kim, Nae-Man Park, Kyung-Hyun Kim, Yong Sung, Young-Woo Ok, Tae-Yeon Seong, and Cheol-Jong Choi. Quantum confinement effect of silicon nanocrystals *in situ* grown in silicon nitride films. *Applied Physics Letters*, 85:5355–5357, November 2004.

[29] Charles Kittel. *Introduction to Solid State Physics*. John Wiley & Sons, Inc, Hoboken, NJ, 2005.

[30] Nobuyoshi Koshida. *Device Applications of Silicon Nanocrystals and Nanostructures*. Springer, New York, NY, USA, 2009.

[31] D. Kovalev, H. Heckler, M. Ben-Chorin, G. Polisski, M. Schwartzkopff, and F. Koch. Breakdown of the k-conservation rule in si nanocrystals. *Physical Review Letters*, 81, September 1998.

[32] David J. Lockwood. *Light emission in silicon: from physics to devices*. Academic Press, Chestnut Hill, Massachusetts, USA, 1998.

[33] Antonio Luque and Steven Hegedus. *Photovoltaic Science and Engineering*. John Wiley & Sons, Inc, West Sussex, England, 2003.

[34] K Ma, J Y Feng, and Z J Zhang. Improved photoluminescence of silicon nanocrystals in silicon nitride prepared by ammonia sputtering. *Institute of Physics Publishing*, 17:4650–4653, August 2006.

[35] Hugh Angus Macleod. *Thin-film Optical Filters*. Institute of Physics Publishing, London, England, 2001.

[36] Umesh K. Mishra and Jasprit Singh. *Semiconductor Device Physics*. Springer, Dordrecht, The Netherlands, 2008.

[37] L. Dal Negro, J. H. Yi, , J. Michel, L. C. Kimerling, T.-W. F. Chang, V. Sukhovatkin, and E. H. Sargent. Light emission efficiency and dynamics in silicon-rich silicon nitride films. *Applied Physics Letters*, 88:29–50, June 2006.

[38] L. Dal Negro, J. H. Yi, M. Hiltunen, J. Michel, L. C. Kimerling, S. Hamel, A. J. Williamson, G. Galli, T.-W. F. Chang, V. Sukhovatkin, and E. H. Sargent. Light-emitting silicon-rich nitride systems and photonic structures. *Journal of Experimental Nanoscience*, 1:29–50, March 2006.

[39] L. Dal Negro, J. H. Yi, L. C. Kimerling, S. Hamel, A. J. Williamson, and G. Galli. Light emission from silicon-rich nitride nanostructures. *Applied Physics Letters*, 88, May 2006.

[40] Jenny Nelson. *The Physics of Solar Cells*. Imperial College Press, London, UK, 2003.

[41] Edward D. Palik. *Electronic Handbook of Optical Constants of Solids*. Academic Press, San Diego, CA, USA, 1999.

[42] Nae-Man Park, Sang Hyeob Kim, Gun Yong Sung, and Seong-Ju Park. Growth and size control of amorphous silicon quantum dots using SiH_4/N_2 plasma. *Chemical Vapor Deposition*, 8, 2002.

[43] David A. Porter, Kenneth E. Easterling, and Mohamed Sherif. *Phase Transformations in Metals and Alloys*. CRC Press, 2009.

[44] Michael Quirk and Julian Serda. *Semiconductor Manufacturing Technology*. Prentice Hall, Upper Saddle River, New Jersey, USA, 2001.

[45] Ohl R.S. Light-sensitive electric device. *U. S. Patent 2402662*, June 1946.

[46] Bahaa E. A. Saleh and Malvin Carl Teich. *Fundamentals of Photonics*. John Wiley & Sons, Inc., New York / Chichester / Brisbane / Toronto / Singapore, 1991.

[47] G. Santana, B. M. Monroy, A. Ortiz, L. Huerta, J. C. Alonso, J. Fandino, E. Hoyos J. Aguilar-Hernandez, F. Cruz-Gandarilla, and G. Contreras-Puentes. Influence of the surrounding host in obtaining tunable and strong visible photoluminescence from silicon nanoparticles. *Applied Physics Letters*, 88, January 2006.

[48] Gregory D. Scholes and Garry Rumbles. Excitons in nanoscale systems. *Nature Materials*, 5:683–697, September 2006.

[49] D. G. Seiler, Alain C. Diebold, Thomas J. Shaffner, R. McDonald, W. M. Bullis, P. J. Smith, and E. M. Secula. *Characterization and Metrology for ULSI Technology 2000*. Springer, New York, NY, USA, 2000.

[50] William Shockley and Hans Queisser. Detailed balance limit of efficiency of p-n junction solar cells. *Journal of Applied Physics*, 32:510–519, March 1961.

[51] Dipendra Sinha. The energy consumption-gdp nexus: Panel data evidence from 88 countries. *Munich RePEc Personal Archive*, November 2009.

[52] I. Tarasov, M. Dybiec, S. Ostapenko, A. Rohatgi, V. Yelundur, and A. M. Gabor. Scanning room temperature photoluminescence in $SiN_x:H$ layers. *The European Physical Journal Applied Physics*, 27, 2004.

[53] P. F. Trwoga, A. J. Kenyon, and C. W. Pitt. Modeling the contribution of quantum confinement to luminescence from silicon nanoclusters. *Journal of Applied Physics*, 83:3789–3794, April 1998.

[54] Minghua Wang, Dongsheng Li, Zhizhong Yuan, Deren Yang, and Duanlin Que. Photoluminescence of si-rich silicon nitride: Defect-related states and silicon nanoclusters. *Applied Physics Letters*, 90, March 2007.

[55] M. V. Wolkin, J. Jorne, P. M. Fauchet, G. Allan, and C. Delerue. Electronic states and luminescence in porous silicon quantum dots: The role of oxygen. *Physical Review Letters*, 82, January 1999.

APPENDIX A

The fit of modelled Ψ and Δ values

The fit of Ψ and Δ for the as-deposited samples can be found in figures A.1-A.7, while the fit for the annealed samples can be found in figures A.8-A.14.

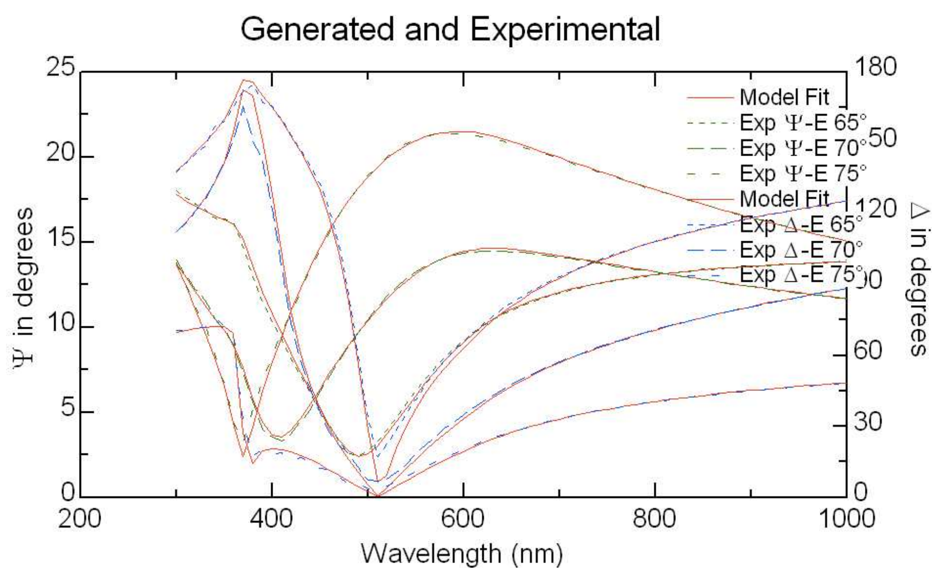

Figure A.1: The fit of Ψ and Δ for ammonia level of 7.8 sccm

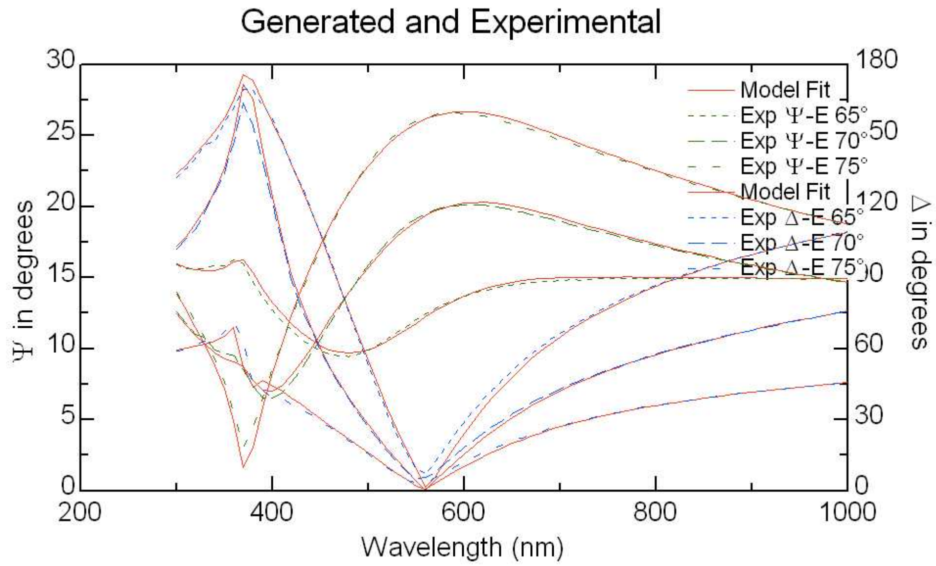

Figure A.2: The fit of Ψ and Δ for ammonia level of 10 sccm

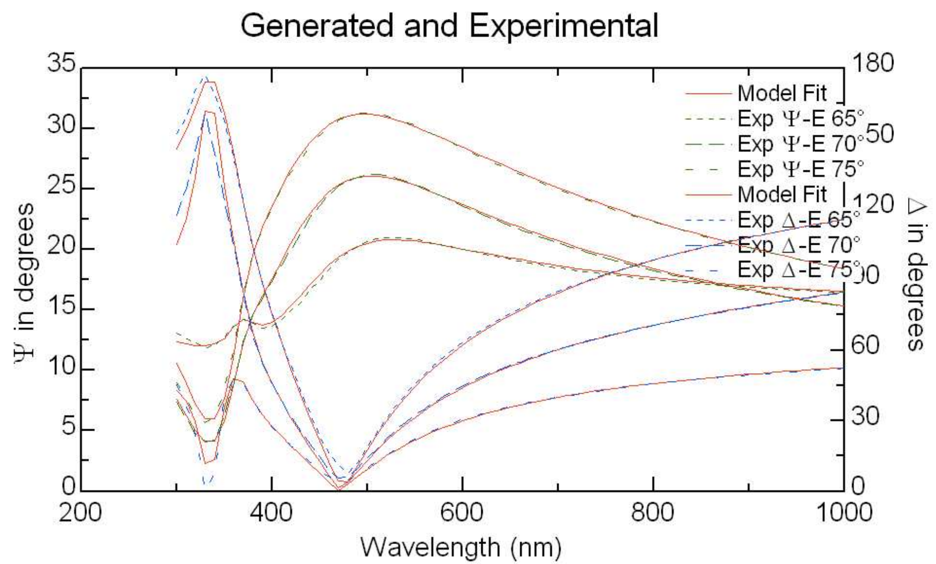

Figure A.3: The fit of Ψ and Δ for ammonia level of 15.6 sccm

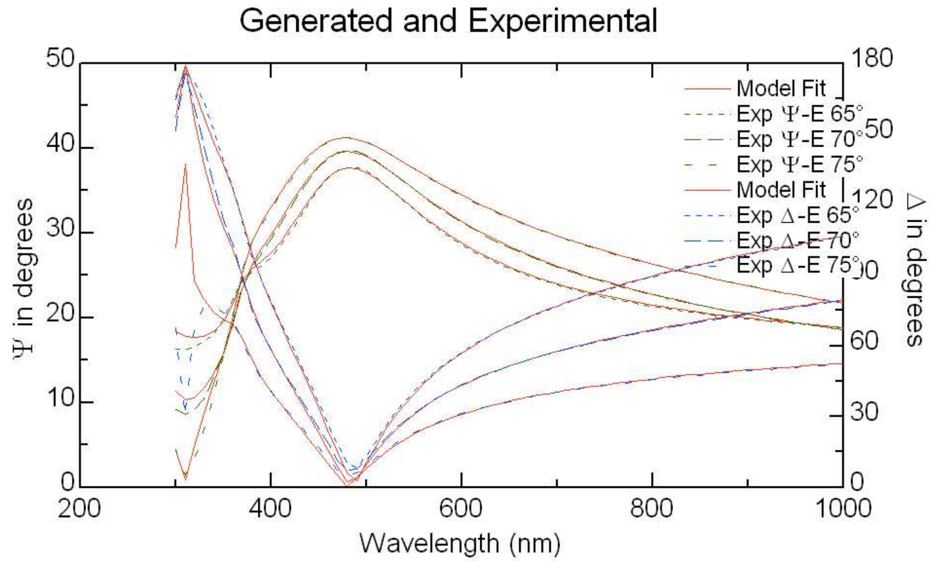

Figure A.4: The fit of Ψ and Δ for ammonia level of 23.4 sccm

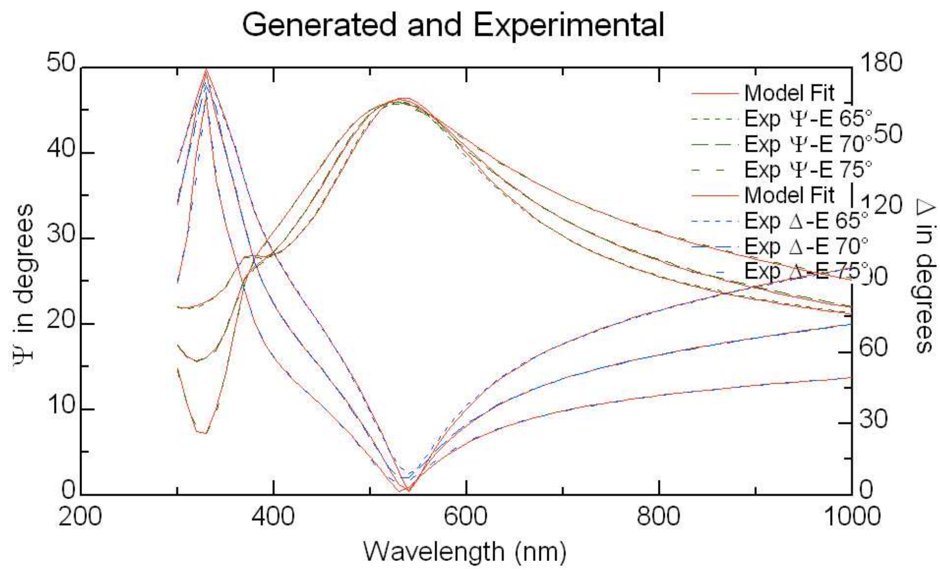

Figure A.5: The fit of Ψ and Δ for ammonia level of 31.2 sccm

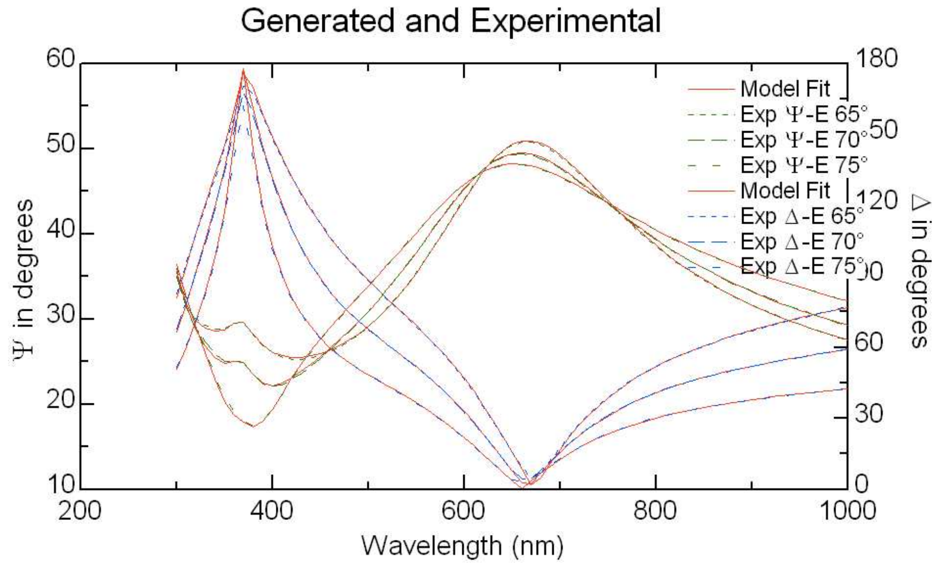

Figure A.6: The fit of Ψ and Δ for ammonia level of 50 sccm

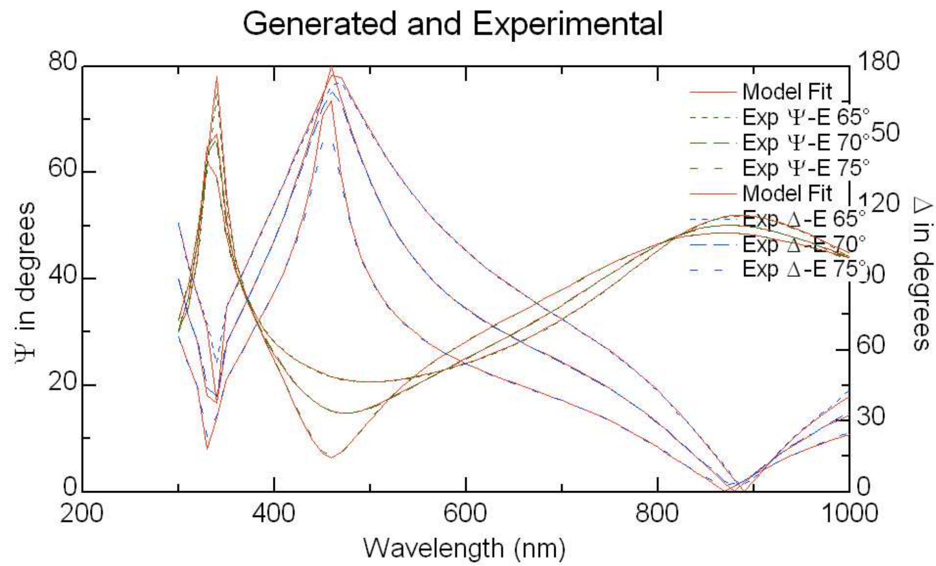

Figure A.7: The fit of Ψ and Δ for ammonia level of 50 sccm and no H_2

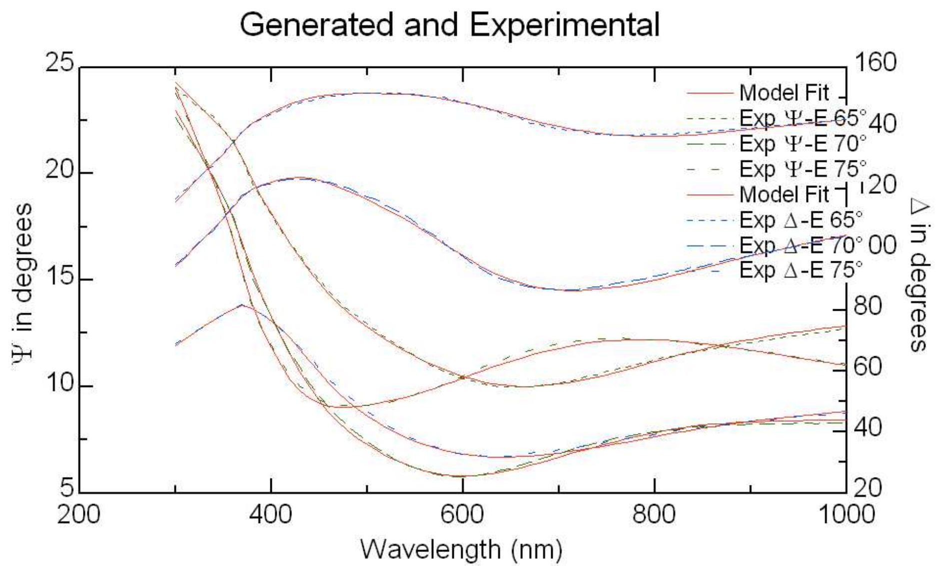

Figure A.8: The fit of Ψ and Δ for ammonia level of 7.8 sccm annealed

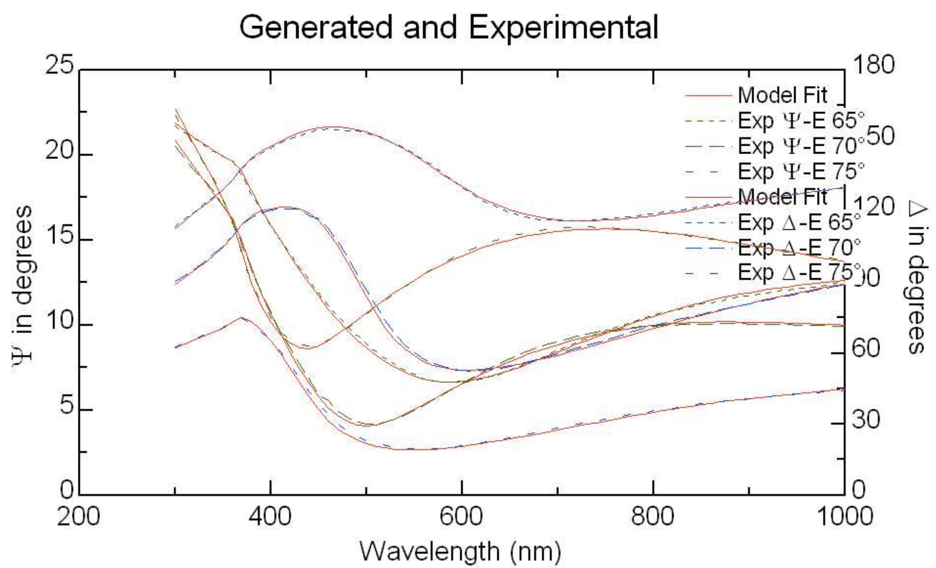

Figure A.9: The fit of Ψ and Δ for ammonia level of 10 sccm annealed

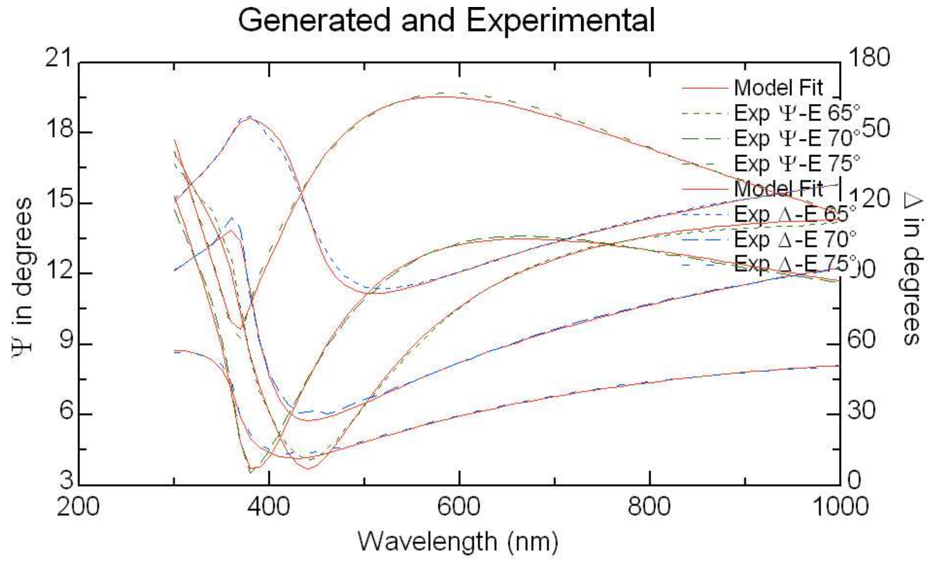

Figure A.10: The fit of Ψ and Δ for ammonia level of 15.6 sccm annealed

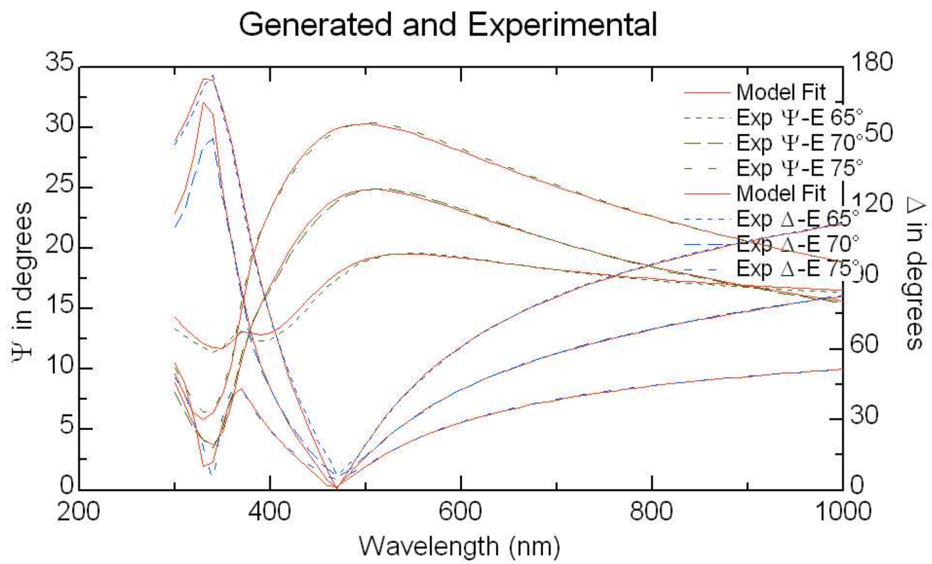

Figure A.11: The fit of Ψ and Δ for ammonia level of 23.4 sccm annealed

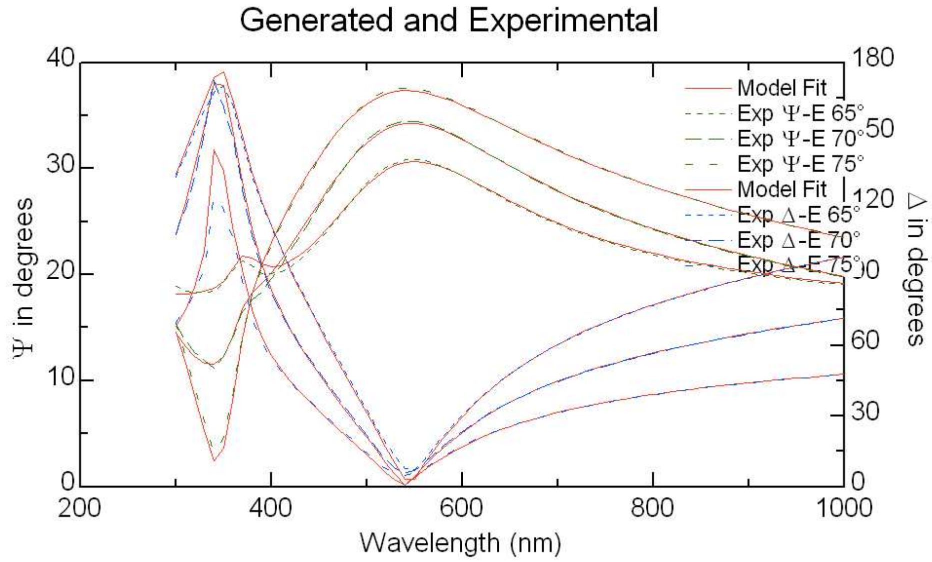

Figure A.12: The fit of Ψ and Δ for ammonia level of 31.2 sccm annealed

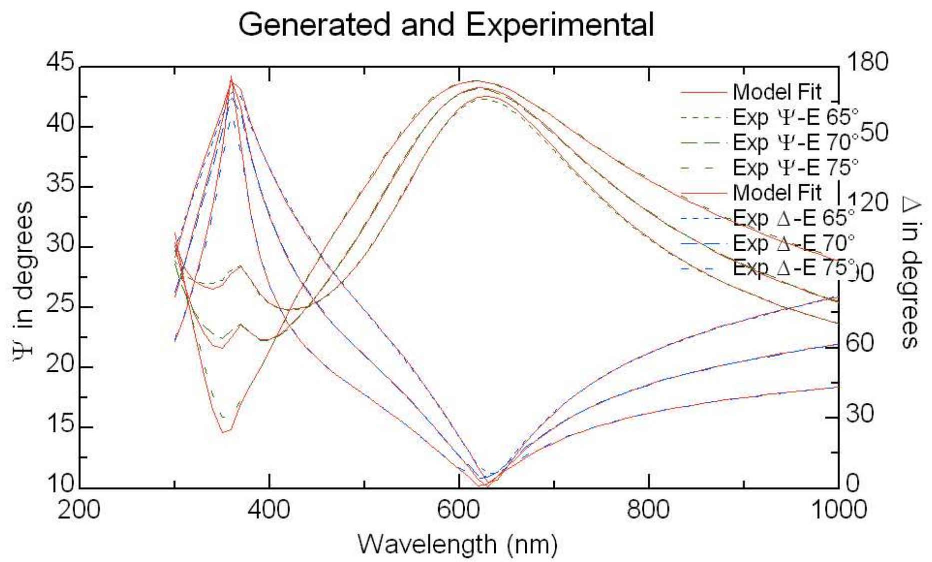

Figure A.13: The fit of Ψ and Δ for ammonia level of 50 sccm annealed

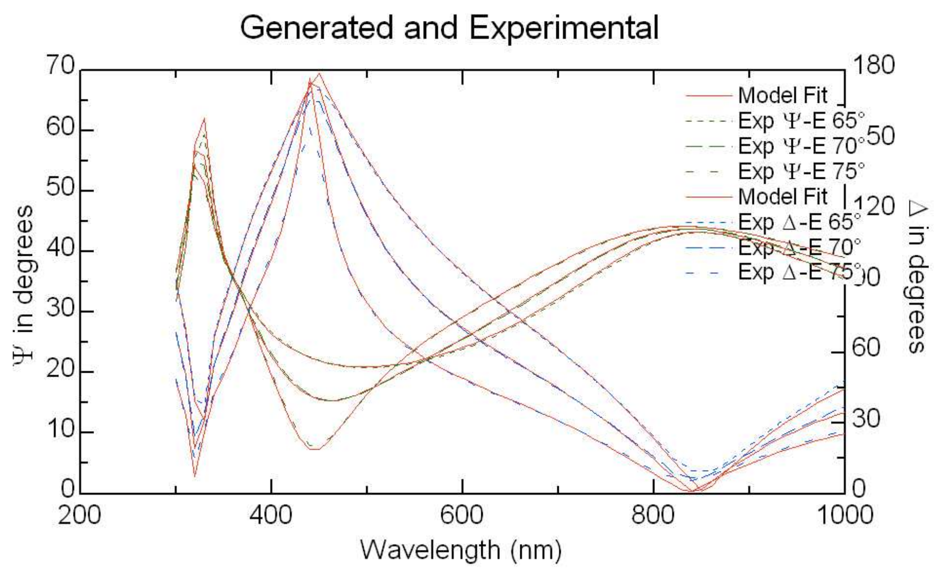

Figure A.14: The fit of Ψ and Δ for ammonia level of 50 sccm and no H_2 annealed

APPENDIX B

Selected results obtained with the ellipsometry model with a BEMA layer consisting of a T-L oscillator, silicon nitride and voids

The fit for Ψ and Δ for selected samples can be found in figures B.1-B.8, while the corresponding index of refraction and extinction coefficient can be found in figures B.9-B.12. Tables B.1 and B.2 contains the final value for the four fittable parameters in the T-L oscillator for the as-deposited and annealed ensembles respectively, while tables B.3 and B.4 contains the final thickness, the weighing of each of the constituents and the MSE.

Table B.1: Final values for the four fittable parameters in the Tauc-Lorentz oscillator for the as-deposited samples (alt. BEMA)

Sample #	A	E_g	E_0	C
1	272.51	2.23	3.53	4.87
4	141.25	2.30	3.89	1.81
5	105.83	2.57	4.41	2.35
6	117.59	3.15	6.24	26.41

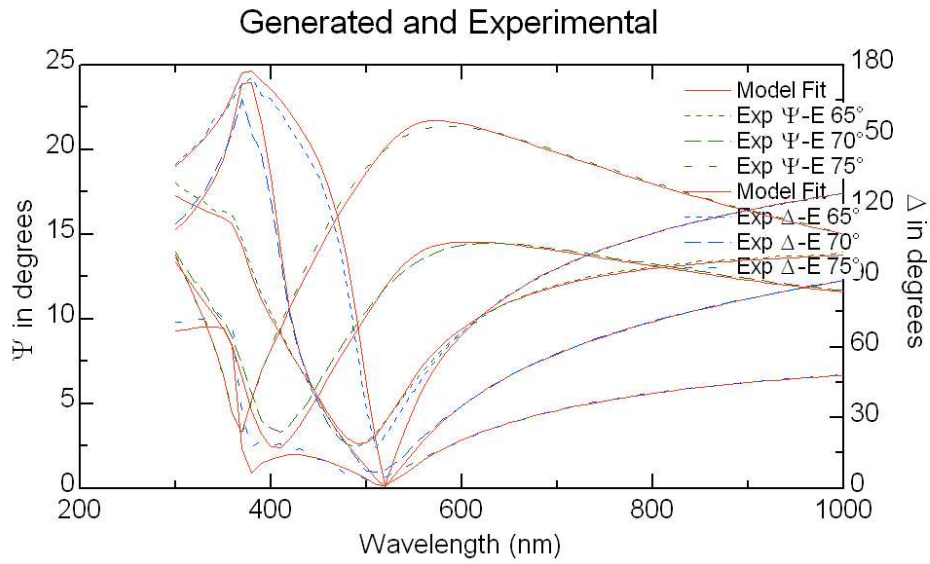

Figure B.1: The fit of Ψ and Δ for ammonia level of 7.8 sccm

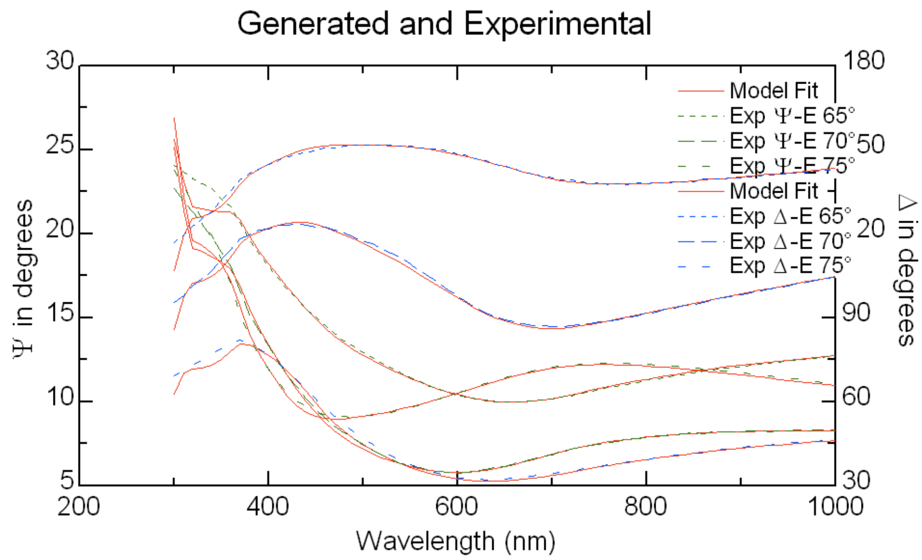

Figure B.2: The fit of Ψ and Δ for ammonia level of 7.8 sccm, annealed

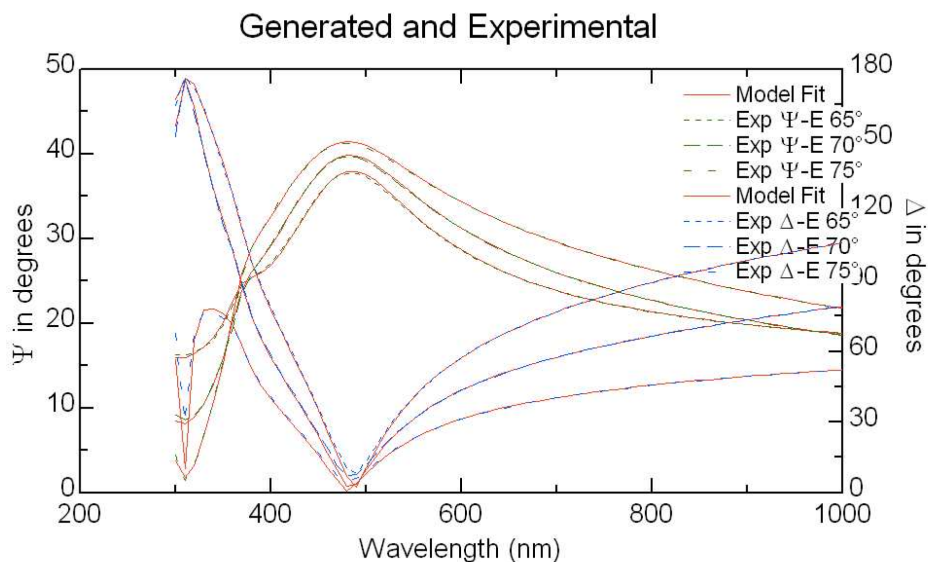

Figure B.3: The fit of Ψ and Δ for ammonia level of 23.4 sccm

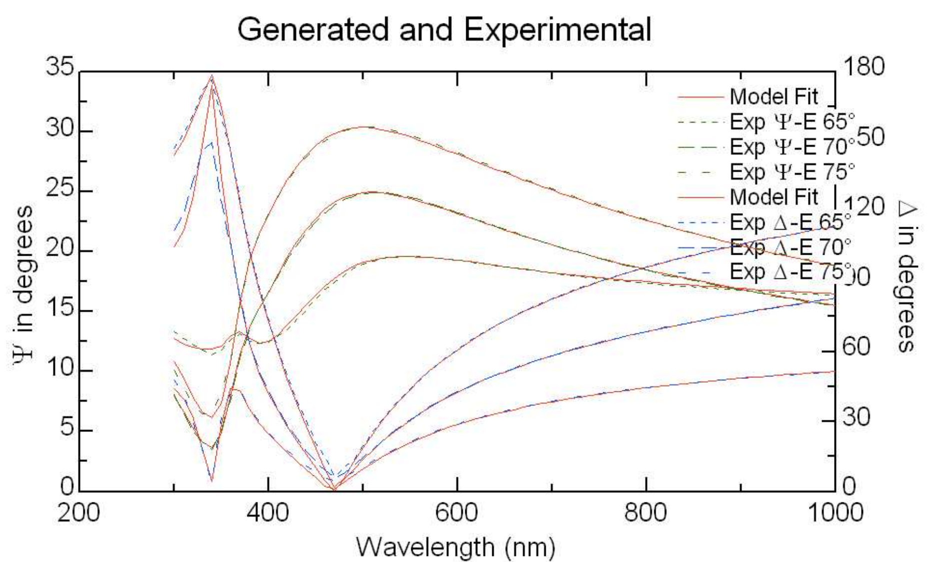

Figure B.4: The fit of Ψ and Δ for ammonia level of 23.4 sccm, annealed

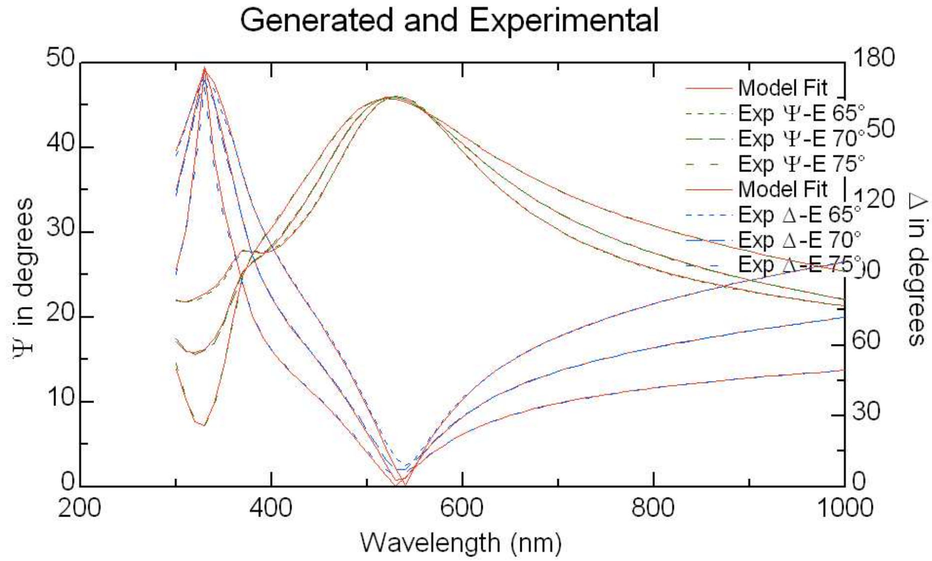

Figure B.5: The fit of Ψ and Δ for ammonia level of 31.2 sccm

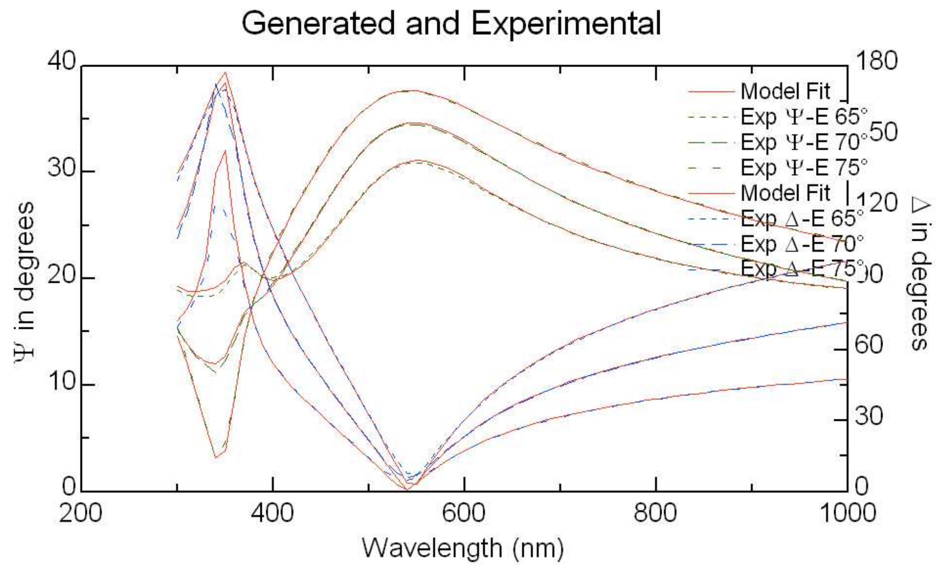

Figure B.6: The fit of Ψ and Δ for ammonia level of 31.2 sccm, annealed

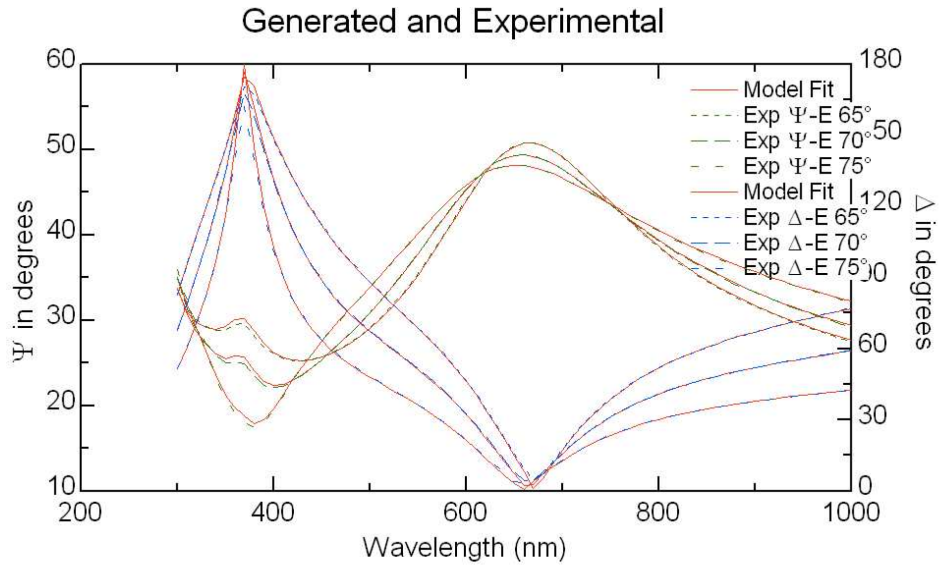

Figure B.7: The fit of Ψ and Δ for ammonia level of 50 sccm

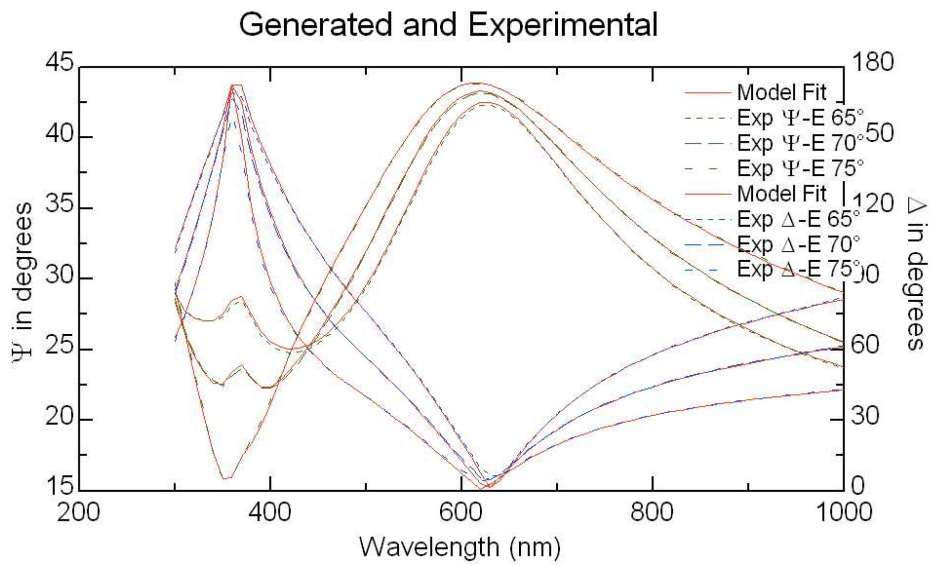

Figure B.8: The fit of Ψ and Δ for ammonia level of 50 sccm, annealed

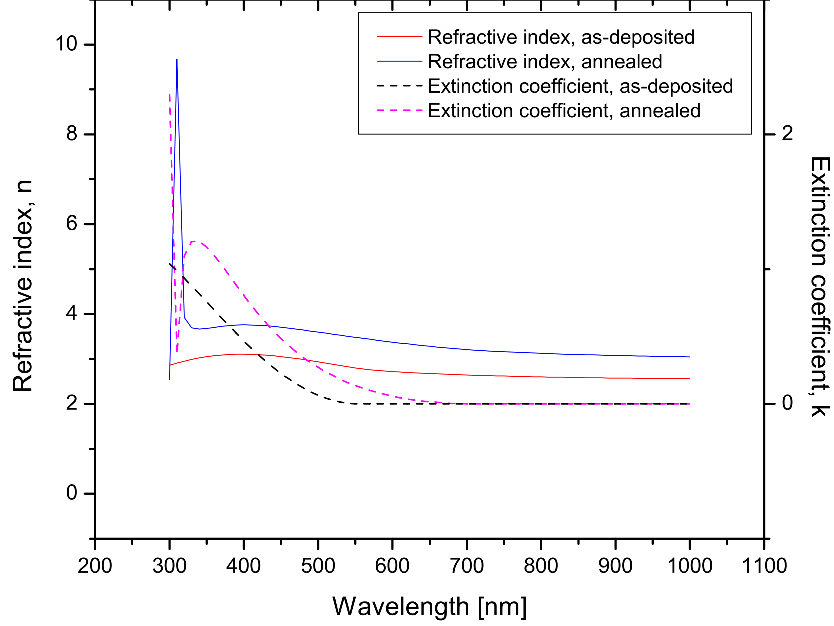

Figure B.9: Refractive index and extinction coefficient for ammonia level of 7.8 sccm

Table B.2: Final values for the four fittable parameters in the Tauc-Lorentz oscillator for the annealed samples (alt. BEMA)

Sample #	A	E_g	E_0	C
1	353.59	1.74	3.61	2.57
4	214.86	1.38	3.39	1.51
5	89.96	2.08	4.21	2.53
6	112.24	2.81	9.88	26.41

Table B.3: Final thickness, weighing of each of the constituents of the alt. BEMA model and MSE for as-deposited samples

Sample #	film thickness [nm]	MSE	*Tauc-Lorentz* (%)	*voids* (%)	*silicon nitride* (%)
1	48	7.15	70.15	-0.42	30.27
4	59	3.71	21.77	13.05	65.18
5	73	4.22	25.32	18.49	56.20
6	100	7.38	46.88	0.93	52.19

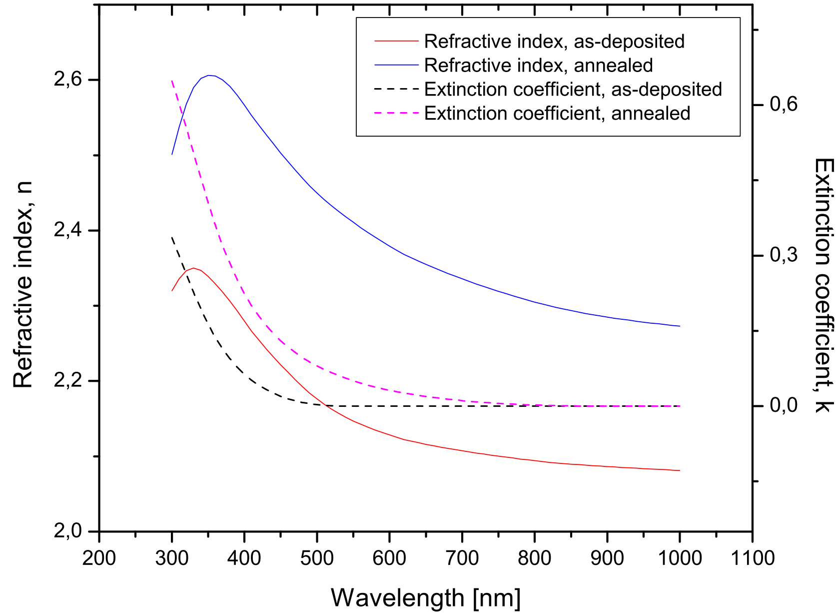

Figure B.10: Refractive index and extinction coefficient for ammonia level of 23.4 sccm

Table B.4: Final thickness, weighing of each of the constituents of the alt. BEMA model and MSE for annealed samples

Sample #	film thickness [nm]	MSE	*Tauc-Lorentz* (%)	*voids* (%)	*silicon nitride* (%)
1	44	12.65	46.27	12.40	41.34
4	52	4.19	20.19	15.80	64.01
5	65	4.76	30.68	15.67	53.65
6	87	6.69	62.67	-3.04	40.37

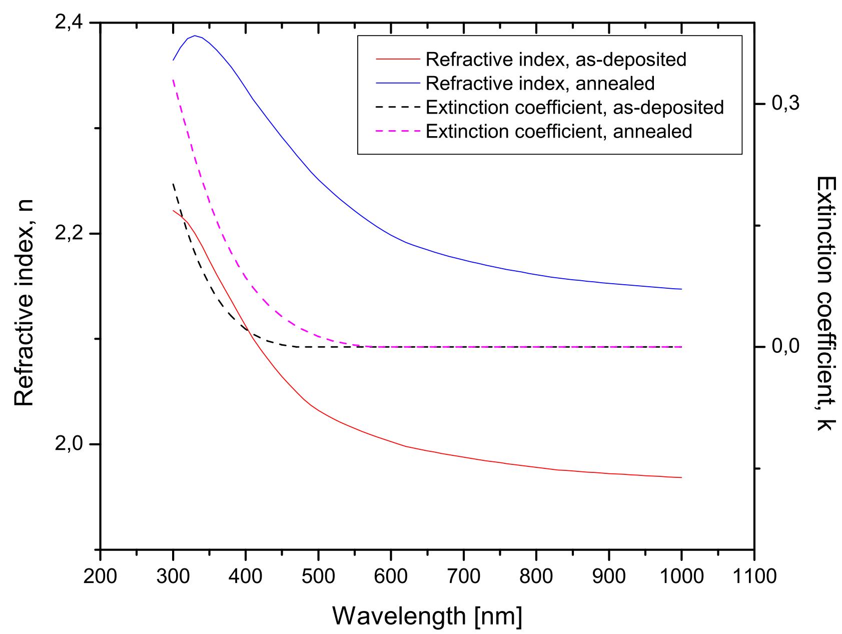

Figure B.11: Refractive index and extinction coefficient for ammonia level of 31.2 sccm

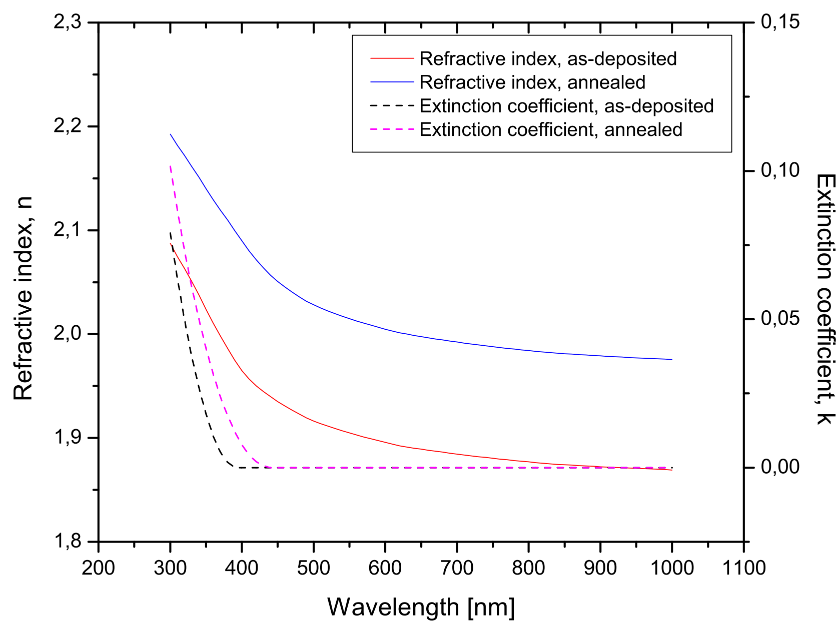

Figure B.12: Refractive index and extinction coefficient for ammonia level of 50 sccm

APPENDIX C

Lifetime measurements for selected samples

Lifetime measurements were carried out for samples that were deposited with film on both sides. No articles of previous work were lifetime measurements have been used in connotation with nanocrystals in a thin film have been found, although there are several articles were the lifetime for thin film silicon nitride is discussed, but it did not seem obvious how this could be related to possible silicon nanostructures in the film. Selected samples have been included anyways for a possible future refrence.

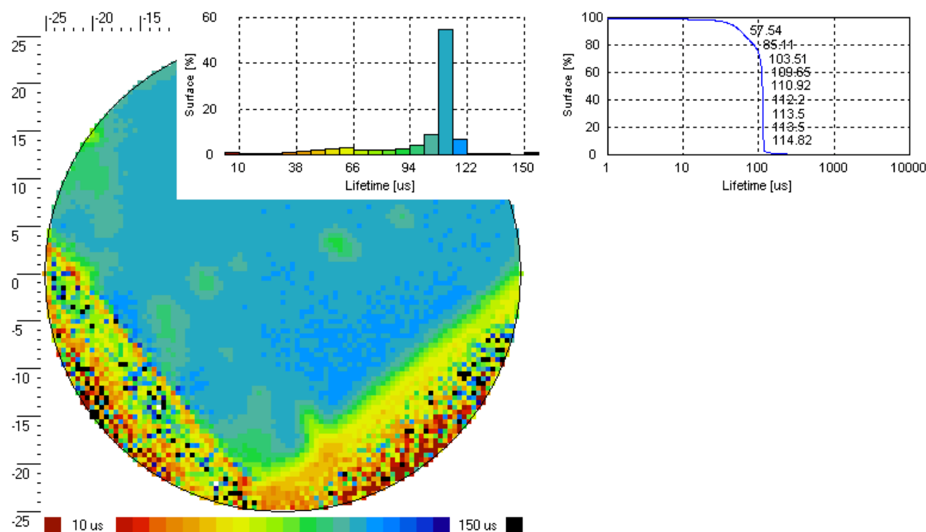

Figure C.1: Lifetime measurement for sample with ammonia level of 7.8 sccm

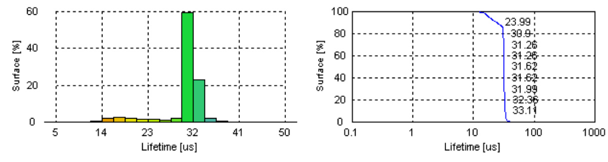

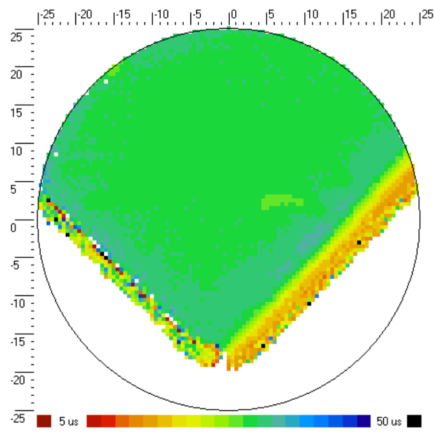

Figure C.2: Lifetime measurement for sample with ammonia level of 15.6 sccm

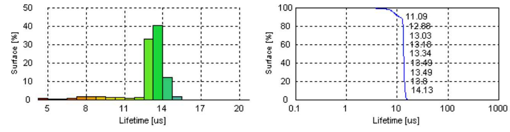

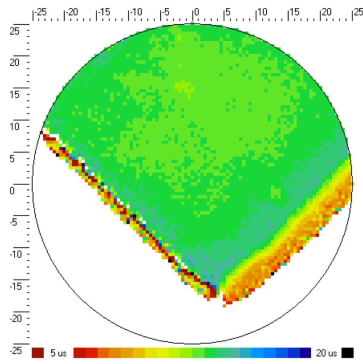

Figure C.3: Lifetime measurement for sample with ammonia level of 23.4 sccm

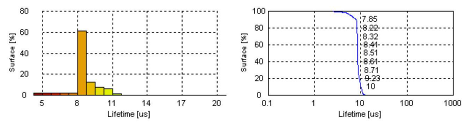

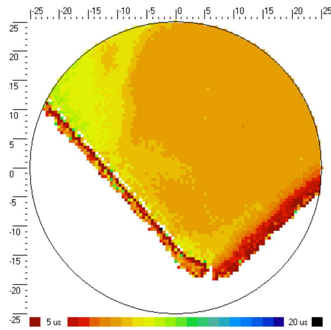

Figure C.4: Lifetime measurement for sample with ammonia level of 31.2 sccm